**Electronic Supplementary Information**

## Section 1. SCXRD information for MIL-53(In)-fum(*c*)

The structure refinement parameters for MIL-53(In)-fum(*c*) from single crystal X-ray diffraction (SCXRD) at 298 K are seen in Table S1.

**Table S1**: Structure refinement parameters for MIL-53(In)-fum(*c*) with DMF as the guest molecule at 298 K.

| MIL-53(In)-fum(*c*) | |
|---|---|
| **Crystal Data** | |
| Chemical Formula Sum | $C_7H_{10}InO_6N$ |
| $M_r$ (g mol$^{-1}$) | 318.98 |
| Crystal System, Space group | Orthorhombic, *Pnma* |
| Temperature (K) | 298 |
| *a*<br>*b*<br>*c*<br>(Å) | 7.307(2)<br>10.626(3)<br>13.915(5) |
| α<br>β<br>γ<br>(°) | 90<br>90<br>90 |
| *V*<br>(Å$^3$) | 1080.4(6) |
| *Z* | 4 |
| *F*(000) | 624 |
| $D_x$<br>(g cm$^{-3}$) | 1.961 |
| Radiation Type | Mo (λ = 0.71073 Å) |
| No. of reflection for cell measurements | 1165 |
| ϑ range (°) for cell measurement | 2.412 – 26.445 |
| μ<br>(mm$^{-1}$) | 2.196 |
| Crystal Shape | Blocks |
| Colour | Colourless |
| Crystal Size (mm$^3$) | 0.2 × 0.028 × 0.028 |
| | |
| **Data Collection** | |
| Diffractometer | Bruker D8 VENTURE<br>Four-circle diffractometer |
| Radiation Source | Mo |
| Detector | Bruker PHOTON II<br>Charge integrating pixel array detector |
| Monochromator | Multilayer Mirror Optics |
| Detector resolution (pixel mm$^{-1}$) | 7.4074 |
| Scan method | Multi-scan |
| Adsorption correction | Multi-scan |

| | |
|---|---|
| $T_{min}$, $T_{max}$ | 0.605, 0.745 |
| Reflections collected | 5946 |
| Independent reflections | 1165 [$R_{int}$ = 0.0511, $R_{sigma}$ = 0.0420] |
| $R_{int}$ | 0.0376 |
| 2θ range for data collection (°) | 4.824 to 52.89 |
| Range of:<br>*h*<br>*k*<br>*l* | <br>-8, 9<br>-12, 13<br>-13, 17 |
| | |
| **Refinement** | |
| Goodness of fit | 1.111 |
| Final R indexes [I>=2σ (I)] | $R_1$ = 0.0362, $wR_2$ = 0.0866 |
| Final R indexes [all data] | $R_1$ = 0.0376, $wR_2$ = 0.0876 |
| No. of reflections | 1165 |
| No. of parameters | 93 |
| No of restraints | 74 |
| H-atom treatment | Mixed |
| Weighting scheme | $w = \frac{1}{\sigma^2(F_o^2) + (0.0187P)^2 + 4.7974P}$<br>where:<br>$P = \frac{F_o^2 + 2F_c}{3}$ |
| $\Delta\rho_{max}$, $\Delta\rho_{min}$ (e Å$^{-3}$) | 1.17, -0.77 |

Computer programs:

SAINT V8.37A (Bruker-AXS, 2016), APEX3 Ver. 2016.9-0 (Bruker-AXS, 2016), Olex2 1.5 (Dolomanov et al., 2009), SHELXL 2018/3 (Sheldrick, 2015), SHELXT 2018/2 (Sheldrick, 2018).

## Section 2. Crystal structures, vector representations, and calculated energies of the isomeric frameworks

We note discrepancies in the fumarate orientations of the framework about a pore between the previously found and our novel MIL-53-fum structures. Visually, we determined 3 different isomers of the framework based on orientations. The structures are shown below in Fig S1.

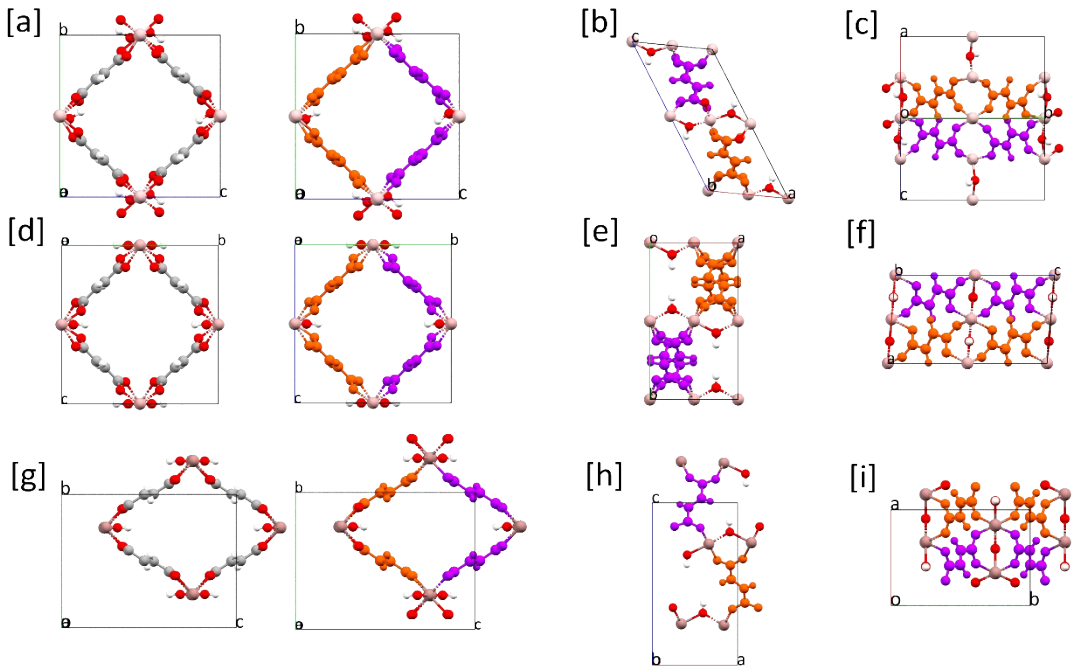


**Figure S1**: Crystal structures of the different isomers of the known MIL-53-fum frameworks. [a], [d], and [g] show a single pore of the frameworks, visible by looking down the a-axis for MIL-53-fum(*a*), MIL-53-fum(*b*), and MIL-53-fum(*c*), respectfully. The purple and orange coloured fumarate linkers indicate the pairs of linkers which lie on the same plane, with the purple linkers lying on a lower plane with a smaller x-coordinate compared to the orange linkers. [b] shows the view of looking down the c-axis for MIL-53-fum(*a*). [e] and [h] show the view of looking the b-axis for the MIL-53-fum(*b*) and MIL-53-fum(*c*) frameworks. [c] shows the view of looking down the b-axis for MIL-53-fum(*a*). [f] and [i] show the view of looking the c-axis for the MIL-53-fum(*b*) and MIL-53-fum(*c*) frameworks.

In [a], [d], and [g] in Fig. S1 the difference in the dimensions of the unit cell and slight variables in the pore shape can be observed. Due to the temporal and spatial averaging nature of PXRD, one can attribute these differences to dynamics as a result from thermal fluctuations. A less obvious detail is the linker orientations as well as the fact that the four fumarate linkers around a pore do not sit in the same plane due to the wine rack stacking structure of these MIL-53-fum frameworks. The difference

in the linker orientation combinations is made more obvious in the two columns to the right in Fig S1. To consider the linker orientation, we use arrows in order to simplify the representation of the fumarate linkers as seen in Fig S2.

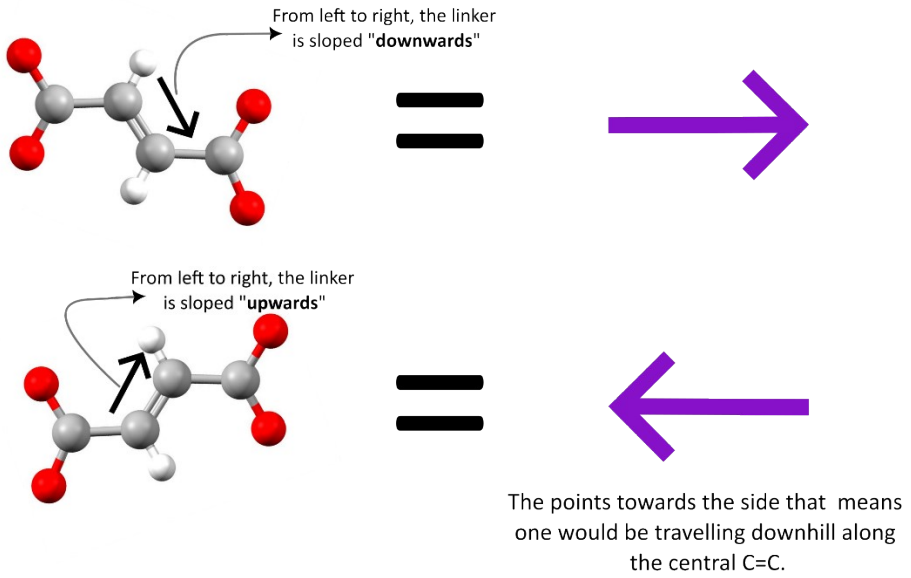


**Figure S2**: Representation on how fumarate linkers are classified as arrows where the orientation is expressed depending on the slope of the C=C double bond in the centre of the linker.

Combining the colour scheme from Fig. S1 and using the convention set in Fig. S2, we can then simplify the crystal structure of the three seen structures. This process is shown in Fig. S3.

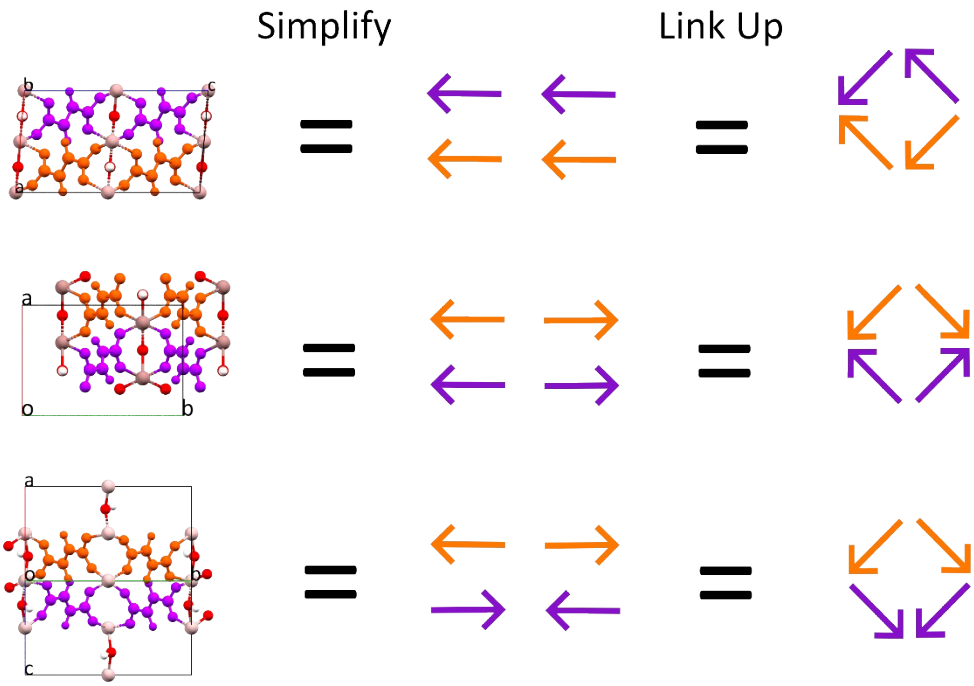


**Figure S3**: Process for simplifying the framework structures to be represented using arrows and colours.

Here we have shown that using a vector diagram to represent the upward or downward orientations of the linkers (see Fig. S2) and the colour to show the planarity of the porous environment, we can decisively distinguish between the three corelated disordered frameworks. To clean up the diagrams, the representations are rotated to align the coplanar linkers (see Fig. S4).

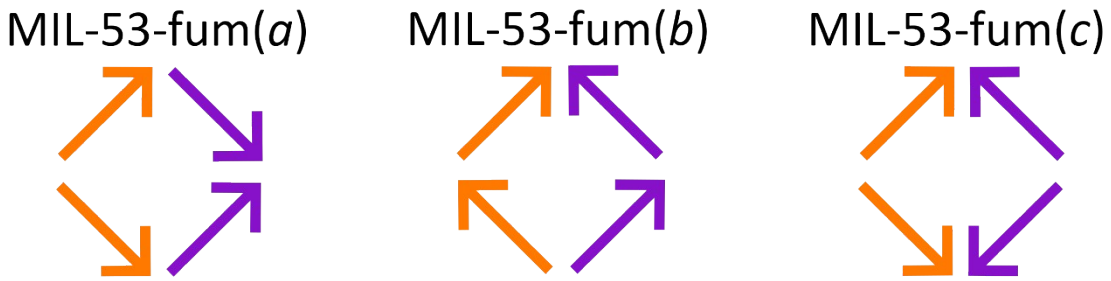


**Figure S4**: Vector diagram showing the three possible correlated disordered structures. The different colours represent the planarity of the linkers. The direction of the arrows denotes the notation of the linker as “up” or “down”. When travelling in the direction of the arrow, one would go “downhill” upon the C=C double bond in the centre of the fumarate linker.

Based on the currently discovered possible structures, two rules for the packing of MIL-53-fum have been established: (1) the number of up and down linkers within a porous environment must be equal to maximise packing efficiency, and (2) the chains of coplanar linkers must remain continuous to

preserve crystallinity. As such, it was concluded that the structure found in this study completes the three possible variations of the linker-based correlated-disordered MIL-53-fum frameworks.

## Section 3. Properties from AIMD simulations of MIL-53(*X*=Sc, Ga, In)-fum(*c*) frameworks

We observe a distinct stabilisation in the gallium analogue in comparison to the scandium or the indium. This is evident by the volume and potential energy of the systems when simulated at standard pressure (0.01 MPa) and temperature (298 K) (see Fig. S5-S7). The differences between the open and closed phases for each isomer is summarised in Table S2.

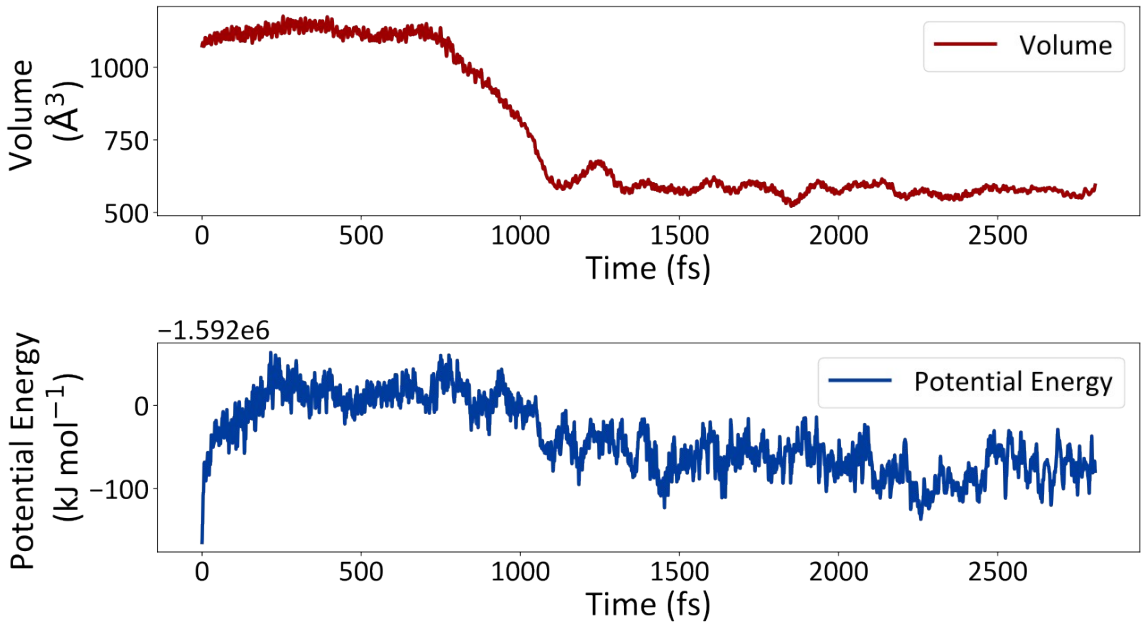


**Figure S5**: Volume (top) and potential energy (bottom) of the simulated unit cell of the scandium analogue of MIL-53-fum(*c*) using the NPT ensemble in an *ab initio* molecular dynamics simulation at ambient temperature and pressure. The volume shows spontaneous closing of the framework which is accompanied by a stabilisation in the potential energy at around 700 fs.

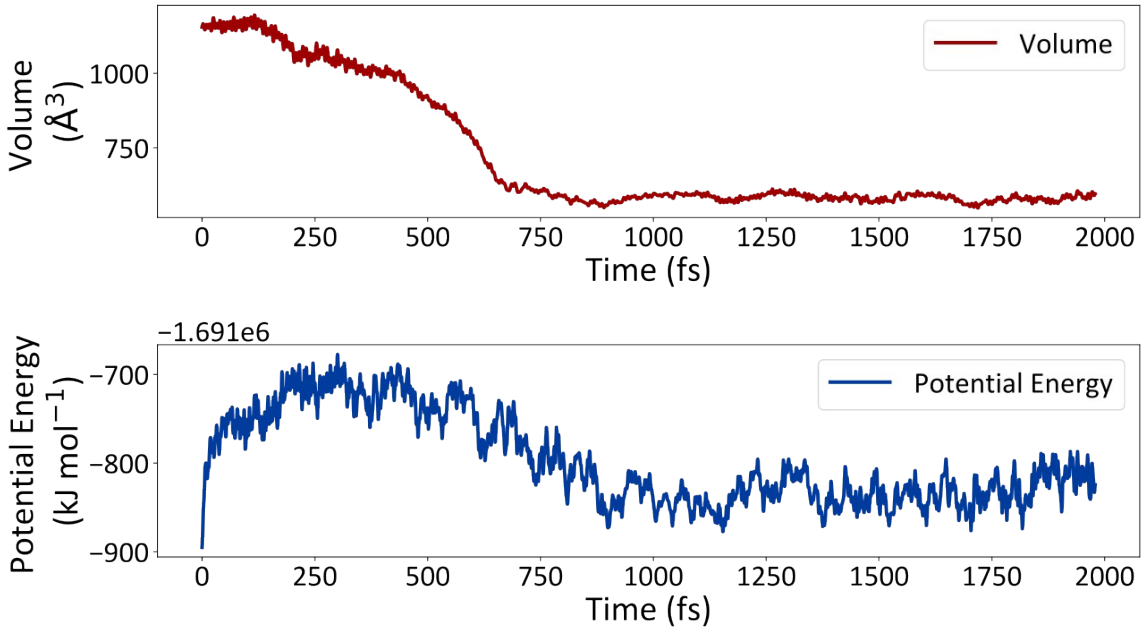


**Figure S6**: Volume (top) and potential energy (bottom) of the simulated unit cell of the indium analogue of MIL-53-fum(*c*) using the NPT ensemble in an *ab initio* molecular dynamics simulation at ambient temperature and pressure. The volume shows spontaneous closing of the framework which is accompanied by a stabilisation in the potential energy, starting at 100 fs.

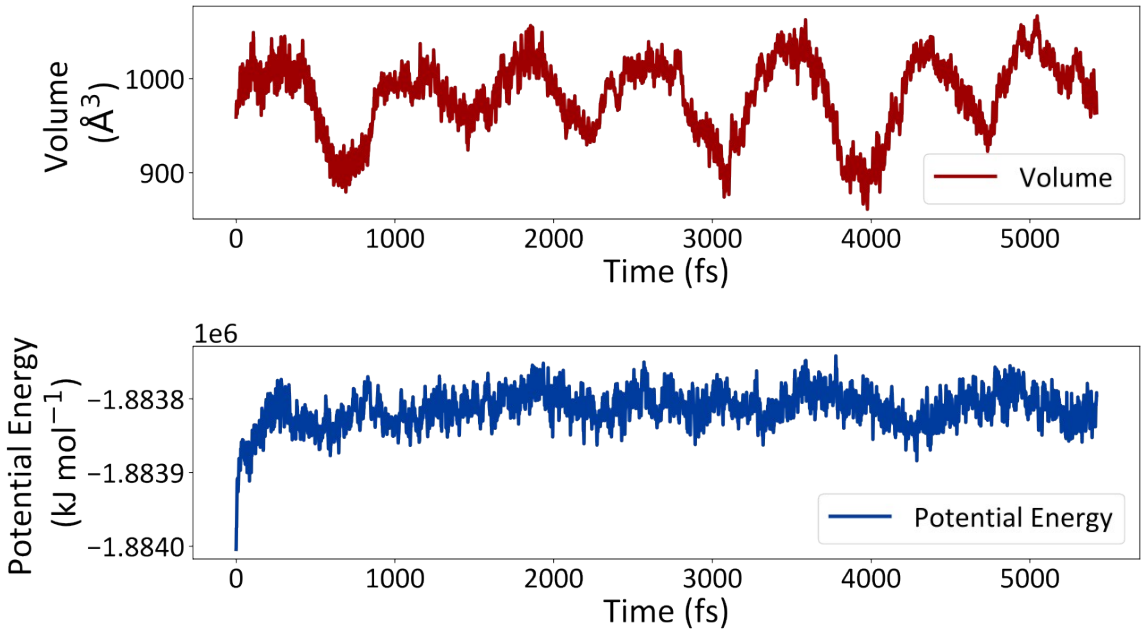


**Figure S7**: Volume (top) and potential energy (bottom) of the simulated unit cell of the gallium analogue of MIL-53-fum(*c*) using the NPT ensemble in an *ab initio* molecular dynamics simulation at ambient temperature and pressure. The volume and potential energy show stability of the open phase of the empty framework.

**Table S2**: Energy and Volume changes from an open- to closed- phases for the MIL-53(X)-fum(*c*) frameworks where X=Sc, Ga, and In. It is noted that the closed structure of the Ga analogue was only accessible at higher pressures (1000 bar). The errors associated with the values are seen in the brackets.

| | **Scandium (ambient)** | | **Gallium (1000 bar)** | | **Indium (ambient)** | |
|---|---|---|---|---|---|---|
| | Potential Energy (kJ/mol) | Volume ($Å^3$) | Potential Energy (kJ/mol) | Volume ($Å^3$) | Potential Energy (kJ/mol) | Volume ($Å^3$) |
| **Open-phase** | -1591980(10) | 1129(20) | -1883810(20) | 982(40) | -16917250(20) | 1075(60) |
| **Closed-phase** | -1592060(20) | 583(20) | -1883880(10) | 532(30) | -1691830(20) | 528(10) |
| **Change (Open-Closed)** | 80(20) | 545(30) | 70(20) | 449(50) | 100(20) | 492(60) |

## Section 4. Properties from AIMD simulations of MIL-53(Ga)-fum(*a*/*b*/*c*) isomers

To show that the correlated disordered structures were indeed different, we run AIMD NPT simulations of each isomeric structure at ambient conditions (298 K, 0.1 MPa) of the Ga analogues (see Fig. S8-S10).

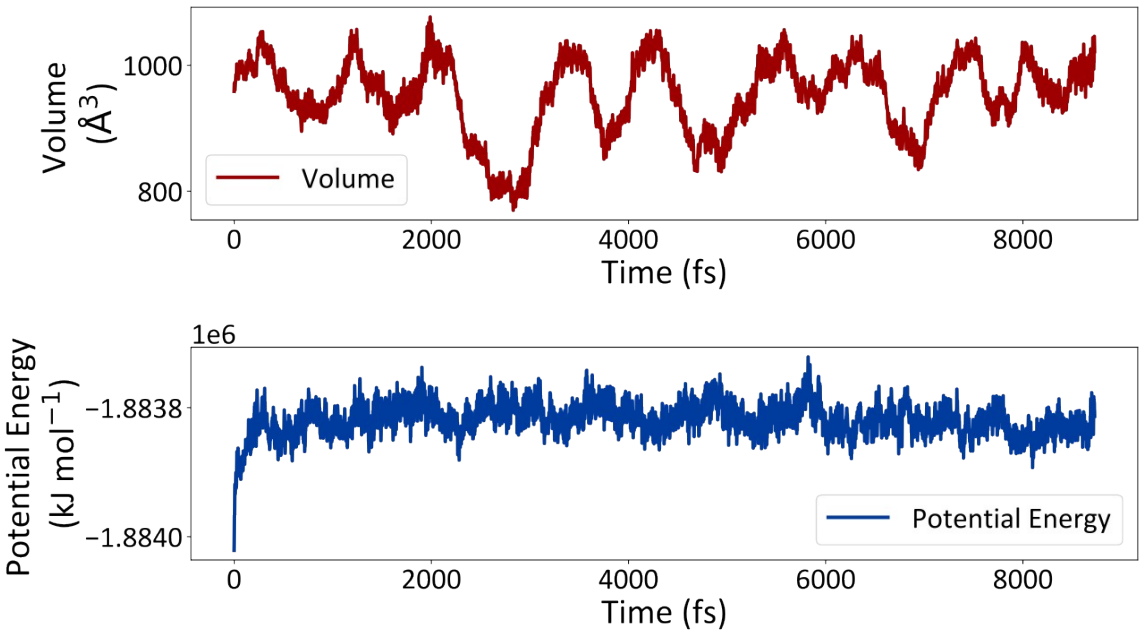


**Figure S8**: Volume (top) and potential energy (bottom) of the simulated unit cell of the gallium analogue of MIL-53-fum(*a*) using the NPT ensemble in an *ab initio* molecular dynamics simulation at ambient temperature and pressure.

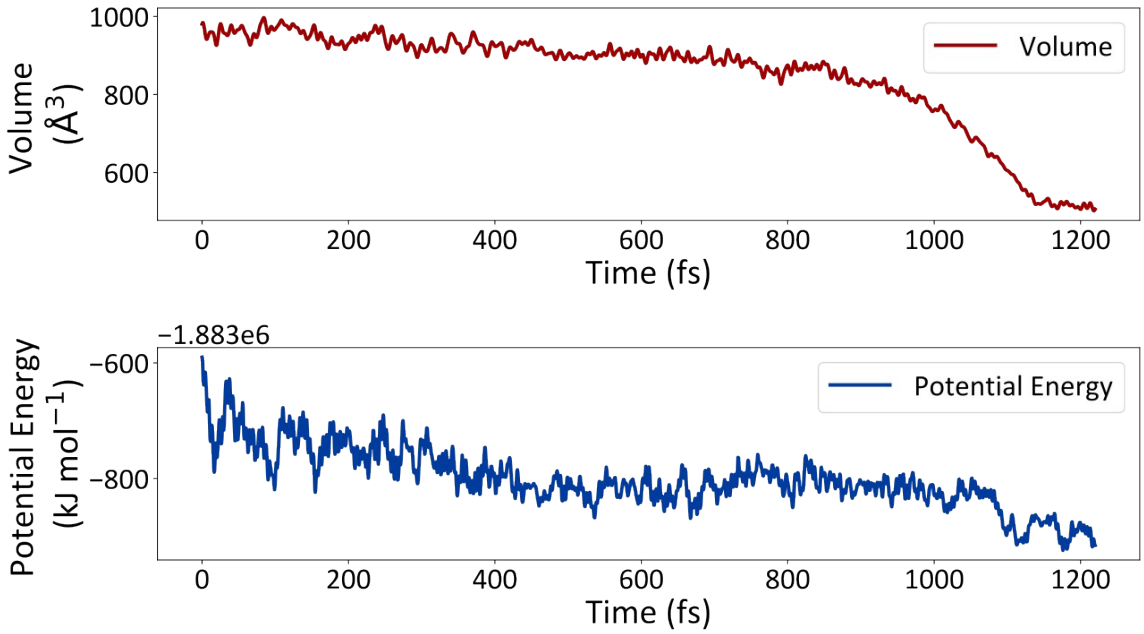


**Figure S9**: Volume (top) and potential energy (bottom) of the simulated unit cell of the gallium analogue of MIL-53-fum(*b*) using the NPT ensemble in an *ab initio* molecular dynamics simulation at ambient temperature and pressure.

**Figure S10**: Volume (top) and potential energy (bottom) of the simulated unit cell of the gallium analogue of MIL-53-fum(*c*) using the NPT ensemble in an *ab initio* molecular dynamics simulation at ambient temperature and pressure.

To compare, the phase transition behaviours of the 3 structures, further MD simulations of the MIL-53(Ga)-fum(*a*) and MIL-53(Ga)-fum(*c*) frameworks were performed at 1000 bar and 298 K. The high pressure ensured that the closed structure was accessible (see Fig. S11 and S12). From the MD outputs of each individual structures, we observe the difference in the stabilisation in potential energy from the opened to the closed phase (see Table S3).

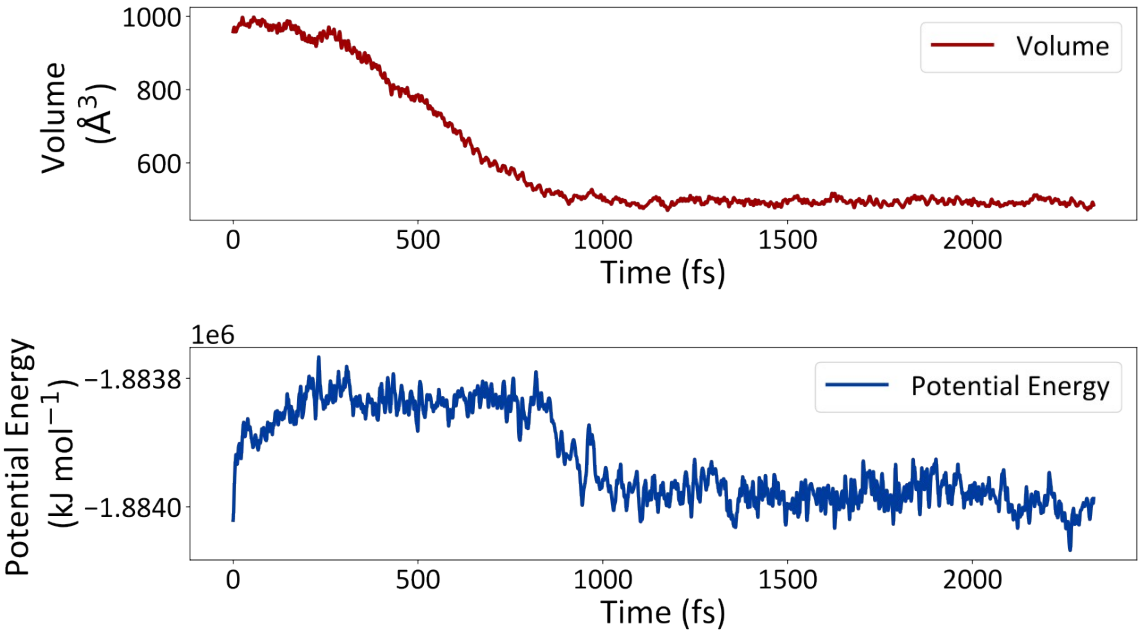


**Figure S11**: Volume (top) and potential energy (bottom) of the simulated unit cell of the gallium analogue of MIL-53-fum(*a*) using the NPT ensemble in an *ab initio* molecular dynamics simulation at ambient temperature and increased pressure of 1000 bar.

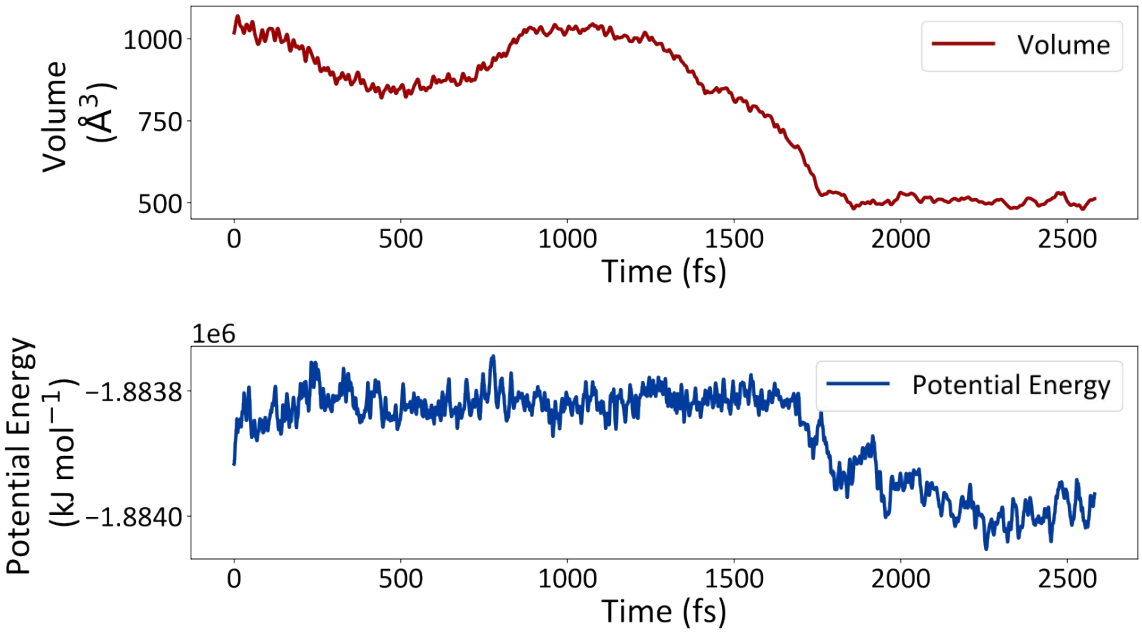


**Figure S12**: Volume (top) and potential energy (bottom) of the simulated unit cell of the gallium analogue of MIL-53-fum(*c*) using the NPT ensemble in an *ab initio* molecular dynamics simulation at ambient temperature and increased pressure of 1000 bar.

**Table S3**: Calculated energies of stabilisation from the opened (op) to closed (cp) phase of structures *a*, *b*, and *c* which differ only by the linker orientation.

| Correlated Disordered Framework | Potential Energy Difference Open- to Closed- Phase (kJ $mol^{-1}$) |
|---|---|
| *a* | -157.35(2) |
| *b* | -212.40(5) |
| *c* | -104.68(6) |

## Section 5. High temperature NPT simulations of MIL-53(Ga)-fum(*c*)

To understand more about the thermal stability of the open phase of structure MIL-53(Ga)-fum(*c*), subsequent simulations of the structure at high temperatures were run. As expected, a steady increase in both potential and kinetic energy was observed with the increase in pressure. From the replicas, it was established that the structure remains in the open phase for temperatures up to 650 K. A run from each of the temperatures are shown in Figure S13.

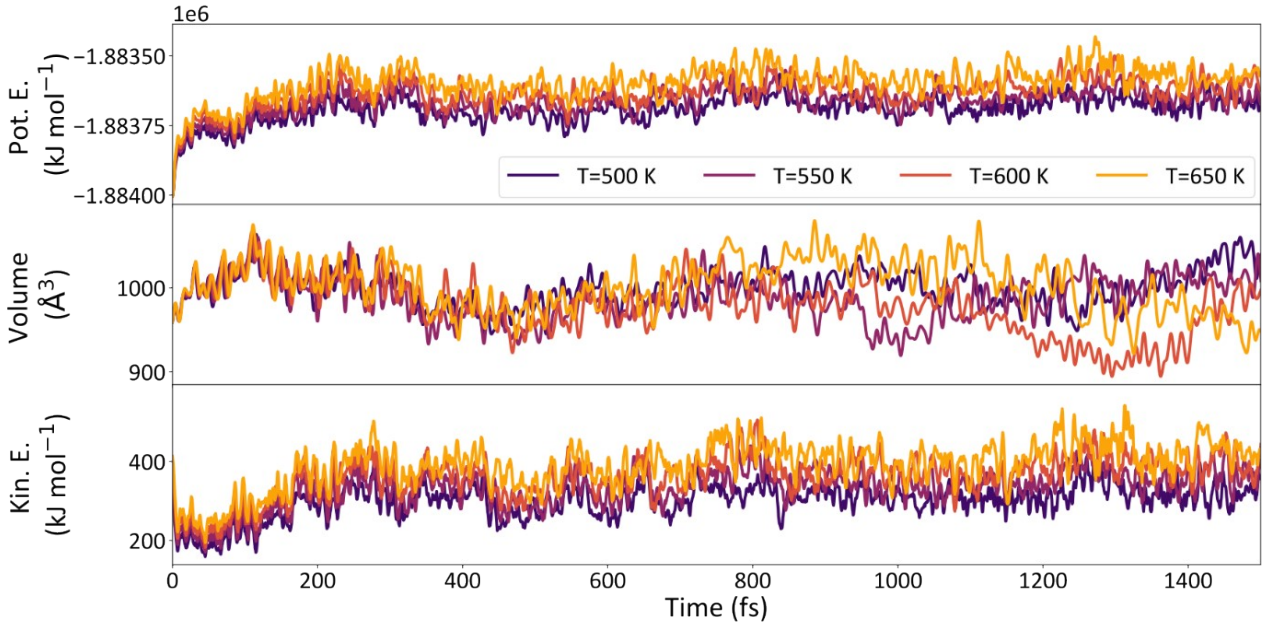


**Figure S13**: *Ab initio* molecular dynamics simulation outputs of the potential energy, volume, and kinetic energy of the MIL-53(Ga)-fum(*c*) system at simulated temperatures of 500, 550, 600, and 650 K and at an ambient pressure of 0.1 MPa.

## Section 6. Potential energy surfaces for MIL-53(Ga)-fum(*c*)

By taking points of equal volume differences along the simulation trajectory of the NPT AIMD at 298 K and 100 MPa, single point energy calculations were performed on each configuration (see Fig. S14). These simulations do not account for any temperature or pressure effects and are effectively performed at 0 K. The implication of such is a potential energy surface with respect to the volume of the system that is purely dependant on the configuration of the system and its containing atoms. As expected, it implies a global minimum of the system when the framework is in the open phase with an extremely high energetic barrier to transition towards the closed phase. Interestingly, we observe that the closed phase in this instance sits in an inflection point rather than a minimum. In conjunction with the surfaces shown in the main text, it can be concluded that the shape and depth of the potential energy surfaces of this framework are highly sensitive to the environmental conditions such as temperature and pressure.

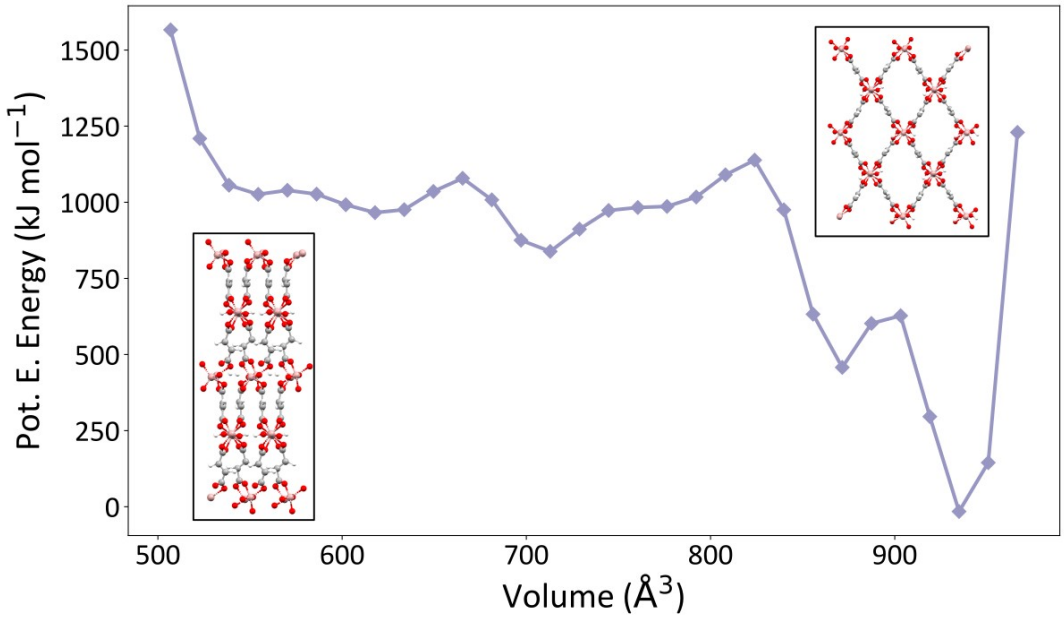


**Figure S14**: The potential energy surface with respects to volume of the MIL-53(Ga)-fum(*c*) framework. Each point represents a single point energy calculation of a configuration going from the open to closed phase, take from the high-pressure NPT simulation. The uncertainties were taken to be the self-consistent field (SCF) convergence limit of the calculations and are shown but not visible against the markers at each point.

## Section 7. Simulated isotherms from GCMC simulations

The simulated isotherms for adsorption of both water and carbon dioxide by MIL-53(Ga)-fum*(c)* at 298 K from the grand canonical Monte Carlo (GCMC) simulations are seen in Fig. S15.

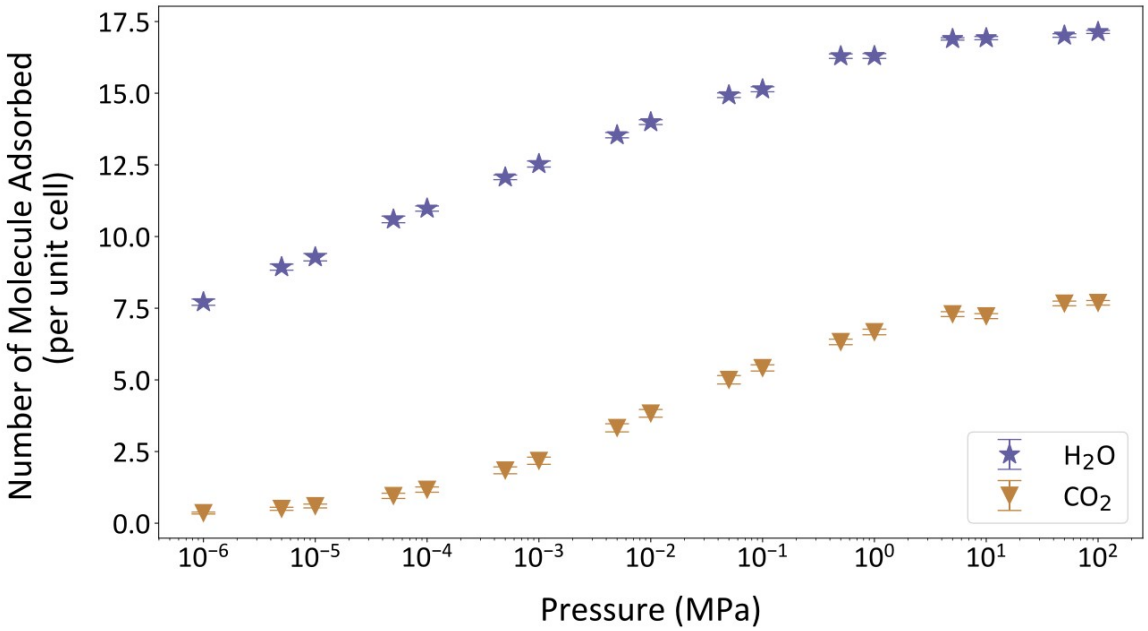


**Figure S15**: Adsorption isotherms of water (blue) and carbon dioxide (orange) into the rigid MIL-53(Ga)-fum(*c*) framework, obtained from GCMC simulations. The error bar originates from the fluctuations of the number of guests adsorbed in each of the GCMC simulations.

## Section 8. Energies from GCMC simulations

For both guest cases, we see an overall reduction in potential energy upon the adsorption of guest molecules. This is a cooperative effect of the stabilisation between the adsorption of guests into the framework, as well as the intermolecular interactions between the guest molecules within the pores of the framework. For water, the intermolecular interactions are likely hydrogen bonding networks being formed by the molecules. Interestingly, at higher pressures, we see an overall destabilisation of the adsorbate-adsorbate energy for water, this is likely due to the fact that when overpacked, the dipoles of the water molecules have a higher chance of being in close proximities and hence an overall destabilisation effect. The plots of the energies with respects to the external pressure for the adsorption of water and carbon dioxide are seen in Fig S16 and S17, respectively.

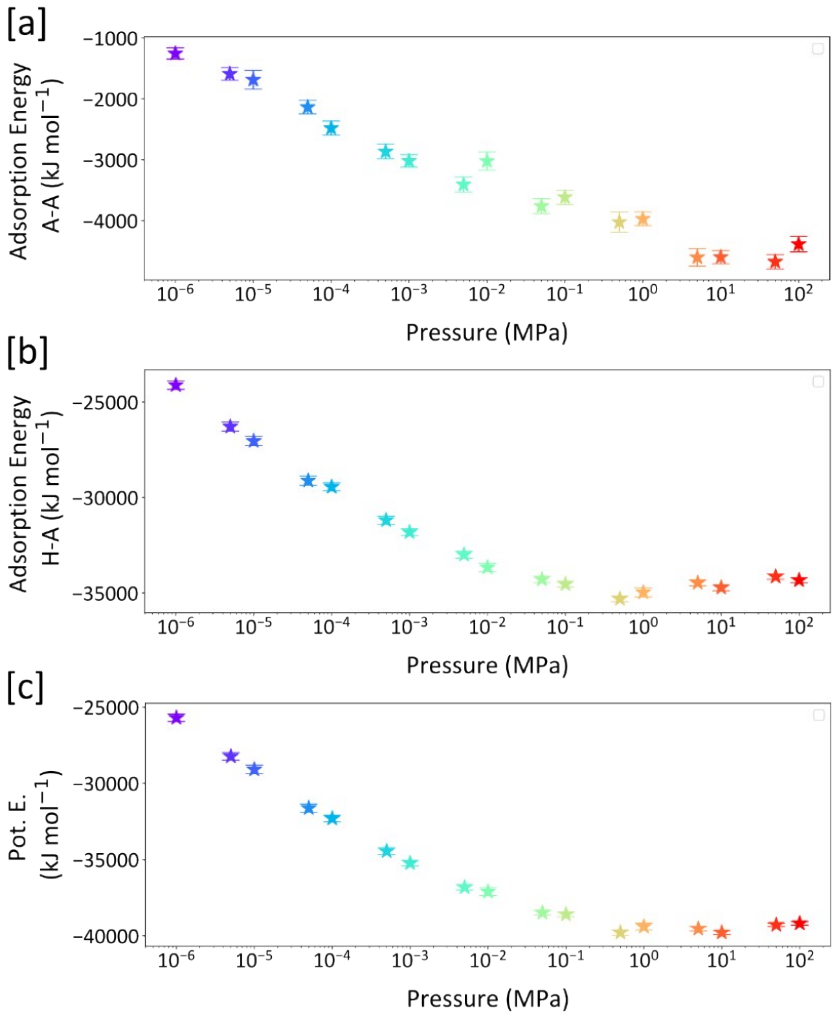


**Figure S16**: Energetic outputs from the production run of the GCMC simulations of a 4x3x3 supercell system of the MIL-53(Ga)-fum(*c*) rigid framework with water adsorption at different pressures. [a] The contribution to the total potential energy that arise from water-water interactions and [b] the contribution from framework-water interactions. [c] The total potential energy of the system. The errors on the plots are smaller than that of the markers for certain points but are plotted for every point.

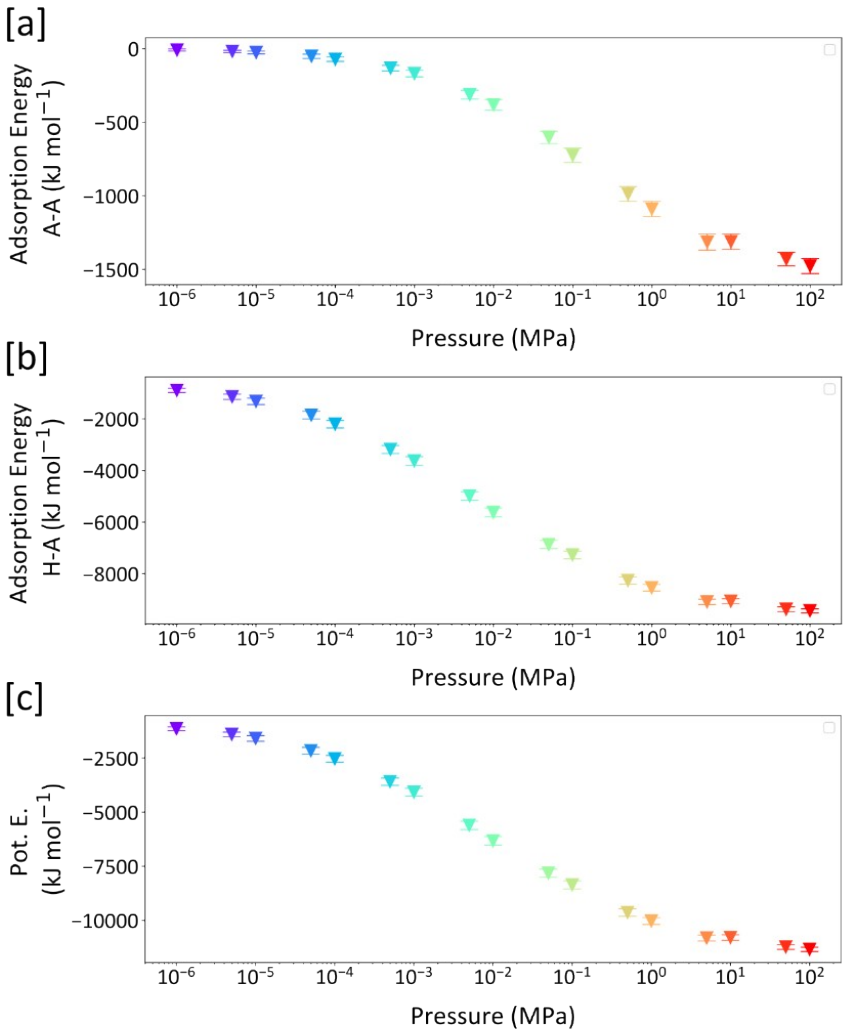


**Figure S17**: Energetic outputs from the production run of the GCMC simulations of a 4x3x3 supercell system of the MIL-53(Ga)-fum(*c*) rigid framework with carbon dioxide adsorption at different pressures. [a] The contribution to the total potential energy that arise from $CO_2$- $CO_2$interactions and [b] the contribution from framework-water interactions. [a] The total calculated potential energy of the system. The errors on the plots are smaller than that of the markers for certain points but are plotted for every point.

## Section 9. Radial distribution functions and hydrogen bonding from GCMC simulations

**Water Adsorption**

The existence of a hydrogen bonding network between the water molecules within the pores of MIL-53(Ga)-fum*(b)* had previously been established from the x-ray crystallography studies by Zhang *et al.*.[1] By calculating the RDF calculated between the oxygen and hydrogen atoms within the water molecules, the effect of increasing the number of water molecules on the strength of the network was probed (see Fig. S18). It was observed that the double peak at 2 to 4 Å represent the hydrogen bond between the oxygen on one water molecule and the two hydrogen atoms on its immediate neighbour. As the pressure increases, we observe a shift in the magnitudes of the double peaks from being equal in size to the one at 4 Å being larger. This would imply a weakening of the overall network as the stronger bond is no longer formed and the larger number of water molecules packing into the pore result in less packing efficiency. From the region of 4 to 12 Å there exist a small loss of peak features with the increase of pressure. This is explained by that fact that with more water molecules, there exist a higher number of random orientations with the water molecules within the pore, which ultimately result in a loss of molecular ordering associated with the hydrogen bonding network. A snapshot showing an example of the hydrogen bonding between the water molecules within the pores of the framework is seen in Fig. S19.

From the RDFs between the hydrogen and oxygen atoms of the water to those of the framework atoms, it is noted that the first peak occurs as a smaller distance for the hydrogen plot compared to the oxygen plot (see Fig. S18). This first indicates that the water coordination is predominantly due to the hydrogen interacting with the oxygen on the hydroxyl site from the framework (see Fig. S18), though there is also evidence of the water oxygen coordinating to both the gallium node and the hydrogen on the hydroxyl group. As the pressure increase, we notice the emergence of new peaks with the hydrogen$_w$-framework RDF in comparison to the loss of features on the oxygen$_w$-framework where imply that new adsorption sites are established for the hydrogens at the loss of that of the oxygens. The oxygens at higher pressure, adsorb into distinct sites at a distance of 3 and 6 Å to the framework.

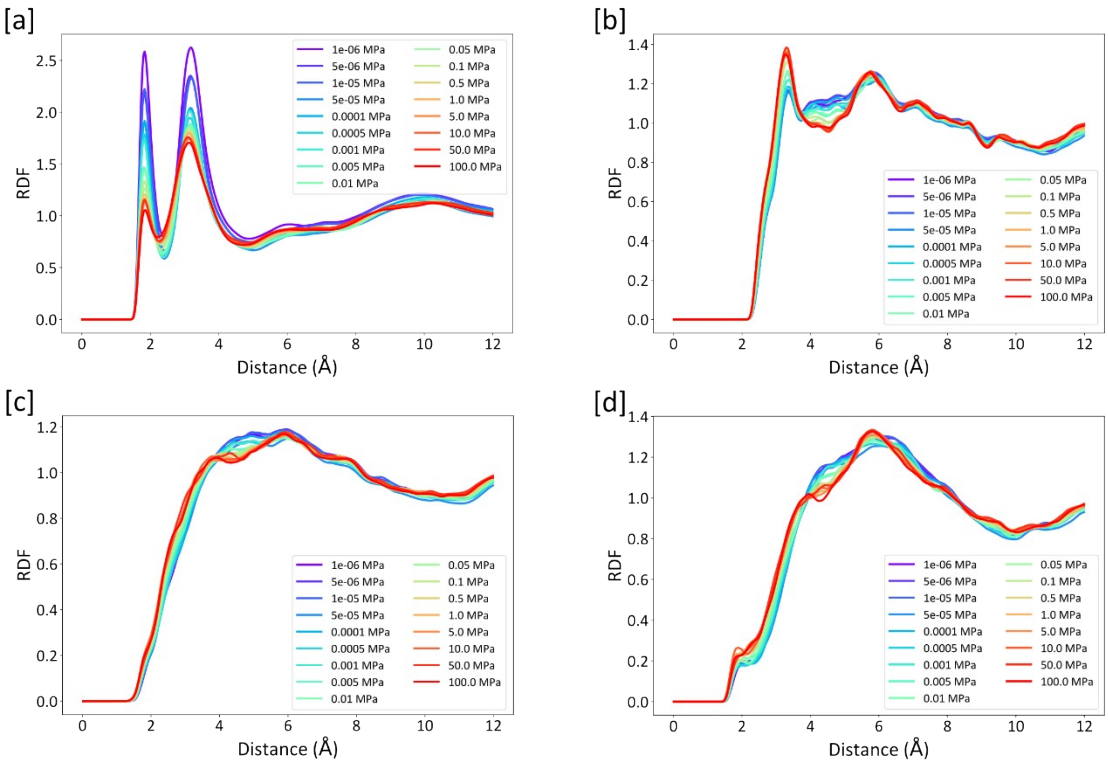


**Figure S18**: Radial Distribution Function (RDF) plots from the GCMC simulations with water as the absorbate at external pressures of $1x10^{-6}$ to 10 MPa for atom pairs of: (a) The hydrogen on the water molecules and oxygen on the water molecules. (b) The oxygen on the water molecules and all of the framework atoms. (c) The hydrogen on the water molecules and the all of the framework atoms. (d) The hydrogen on the water molecules and the oxygen atoms on the framework.

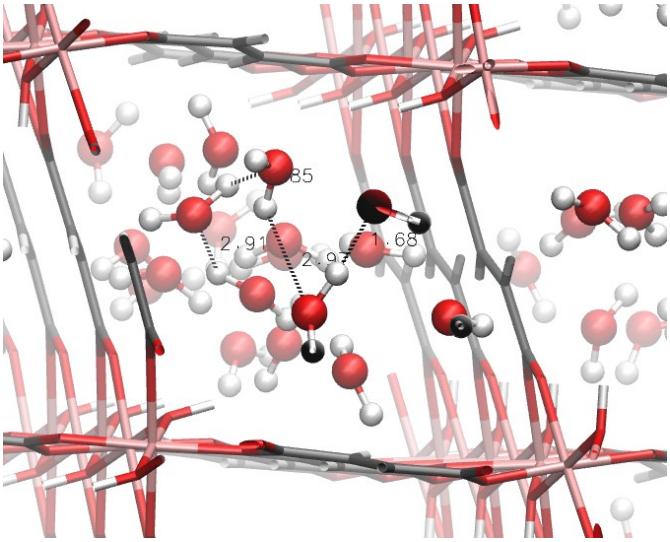


**Figure S19**: Snapshot from the GCMC simulations showing the intermolecular hydrogen bonds which form between the water molecules within the pores of the framework.

**Carbon Dioxide Adsorption**

Similar to the case with the water molecules, the intermolecular interaction between the $CO_2$ molecules were probed by looking at the RDFs of the carbon and oxygen atoms from the guest molecules. Immediately, a small amount of long-range order was observed at the lower pressures which dissipated with higher pressures (see Fig. S20). As speculated from the isotherms, this is simply due to the lack of a permanent dipole in $CO_2$ and hence not forming as strong as a hydrogen-bonding network as water.

The proximity of the $CO_2$ to the framework showed a similar distance for both the carbon and the oxygen (see Fig. S20). It is noted that an increase of feature is present for both RDF plots with the increase of pressure which indicates the emergence of new adsorption sites. The iconic distance between the oxygen atoms from the same $CO_2$ molecule can be seen more evidently from 0.5 MPa as the peaks at approximately 3 and 6 Å become apparent.

The most prominent adsorption site for both the carbon and the hydrogen was identified to be the hydrogen atoms within the framework (see Fig S20). Again, an increase of features on the RDF plot was found to be associated with the increase of pressure. This ordering of the $CO_2$ molecules about the hydrogen atoms of the framework is likely due to the increase in packing of the $CO_2$ molecules within the pores.

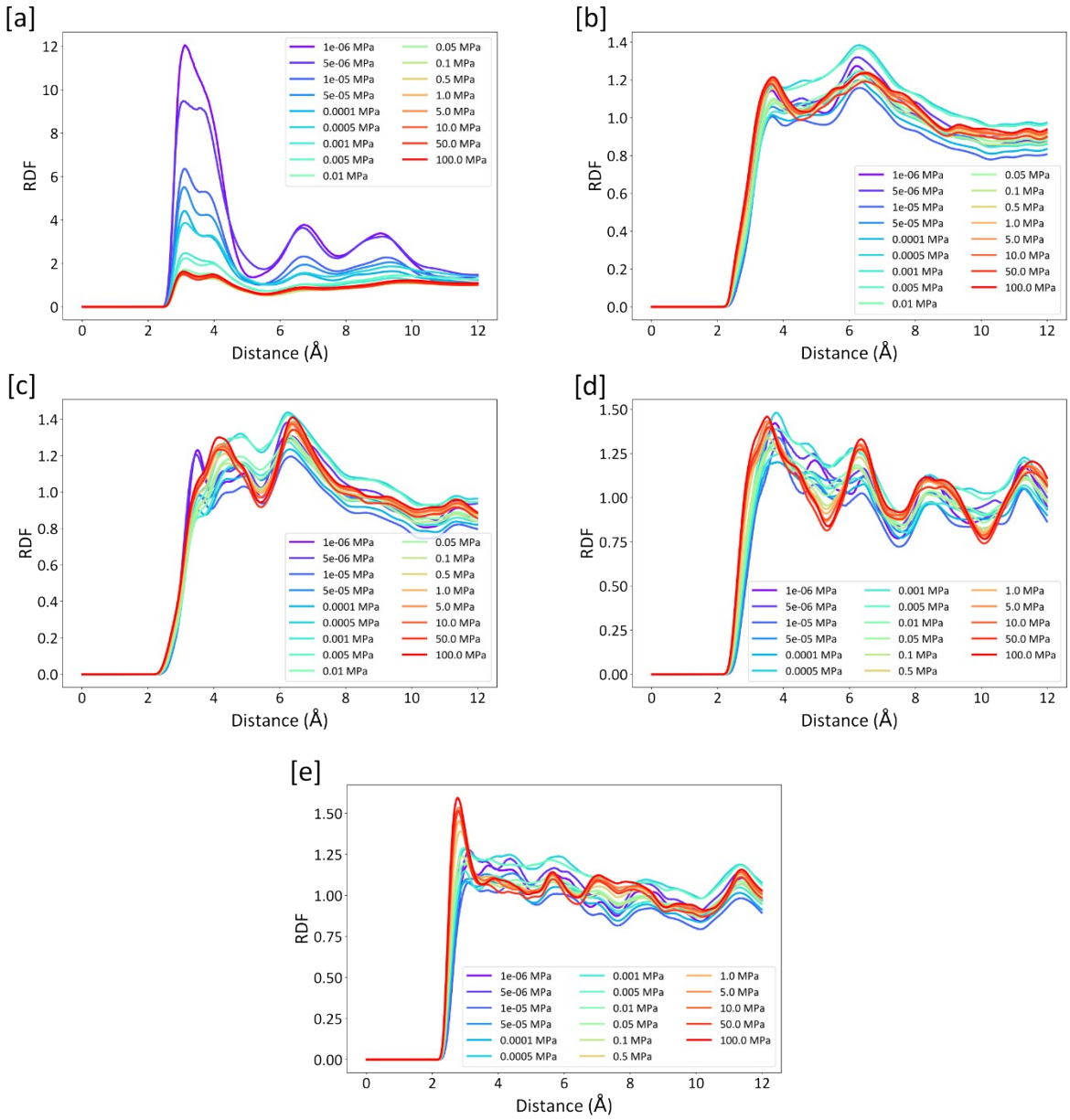


**Figure S20**: Radial Distribution Function (RDF) plots from the GCMC simulations with carbon dioxide as the absorbate at external pressures of $1x10^{-6}$ to 10 MPa for atom pairs of: (a) The carbon on the $CO_2$ molecules and the oxygen on the $CO_2$ molecules. (b) The oxygen on the $CO_2$ molecules and all of the framework atoms. (c) The carbon on the $CO_2$ molecules and all of the framework atoms. (d) The carbon on the $CO_2$ molecules and the hydrogen atoms on the framework. (e) The oxygen on the $CO_2$ molecules and the hydrogen atoms on the framework

## Section 10. Convergence of GCMC simulation

As the simulation of water adsorption has always been known to be temperamental with large fluctuations, it was significant that the equilibration of the system was confirmed and that an appropriate number of sampling points were chosen when it came to deriving crucial properties such as the enthalpy and entropy of adsorption. Here, we adapt a sliding window average method to determine how the calculated enthalpy values would differ depending on where in the simulation the values were taken from (starting point) and the number of data points take from the starting point (window size). This was done with both the water and carbon dioxide systems (Fig. S21 and S23).

The uncertainties that were propagated from the standard deviation of the potential energy of the system as well as the number of guests adsorbed are seen below for water and carbon dioxide (see Fig. S22 and S24).

From Fig. S21 and S23, the temperamental nature of water was evident compared to that of carbon dioxide. Though for both, we observe the expected downwards trend of the heat of adsorption with increasing pressures, the convergence of the values to that trend was immediate obvious even at the beginning of the production run for carbon dioxide. On the other hand, this trend is only more noticeable towards the end of the production run for water.

Interestingly, there are no clear correlations between the uncertainties in the enthalpies with respects to the window size nor stage in production run for either guest molecule systems. The most obvious trend for the uncertainty was the increase with pressures but that was expected as larger systems were seem to have large fluctuations in the number of adsorbed guest molecules.

For each system, the window size was chosen as to minimise the variance in the values between the windows towards the end of the production runs. For water this was a window size of 50, which includes 50,000 MC steps and for carbon dioxide, a window size of 400, corresponding to 400,000 MC steps were chosen.

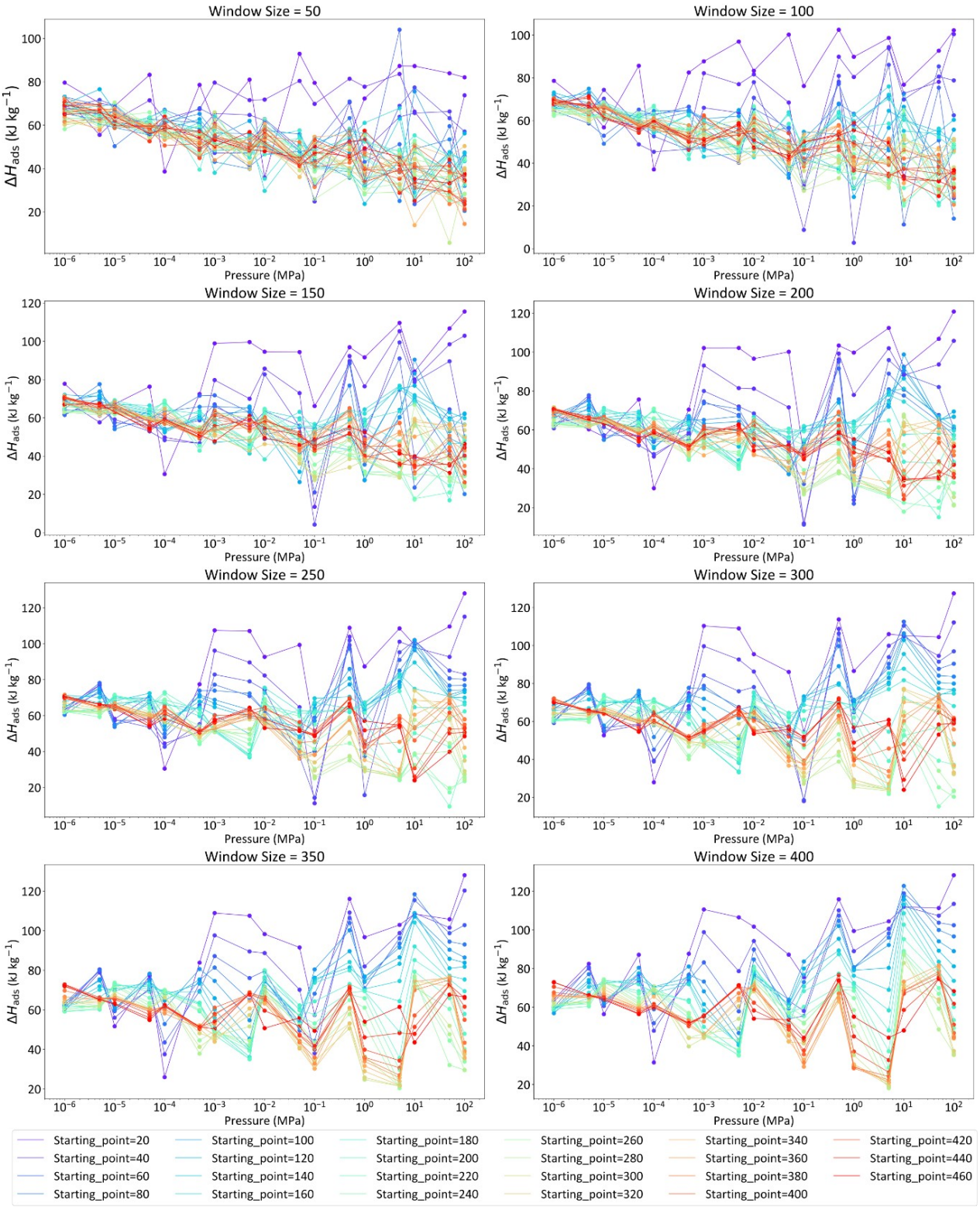


**Figure S21**: Calculated enthalpies of adsorption of water based on the number of data points considered (window size) and the part of the production run that the data points were taken from.

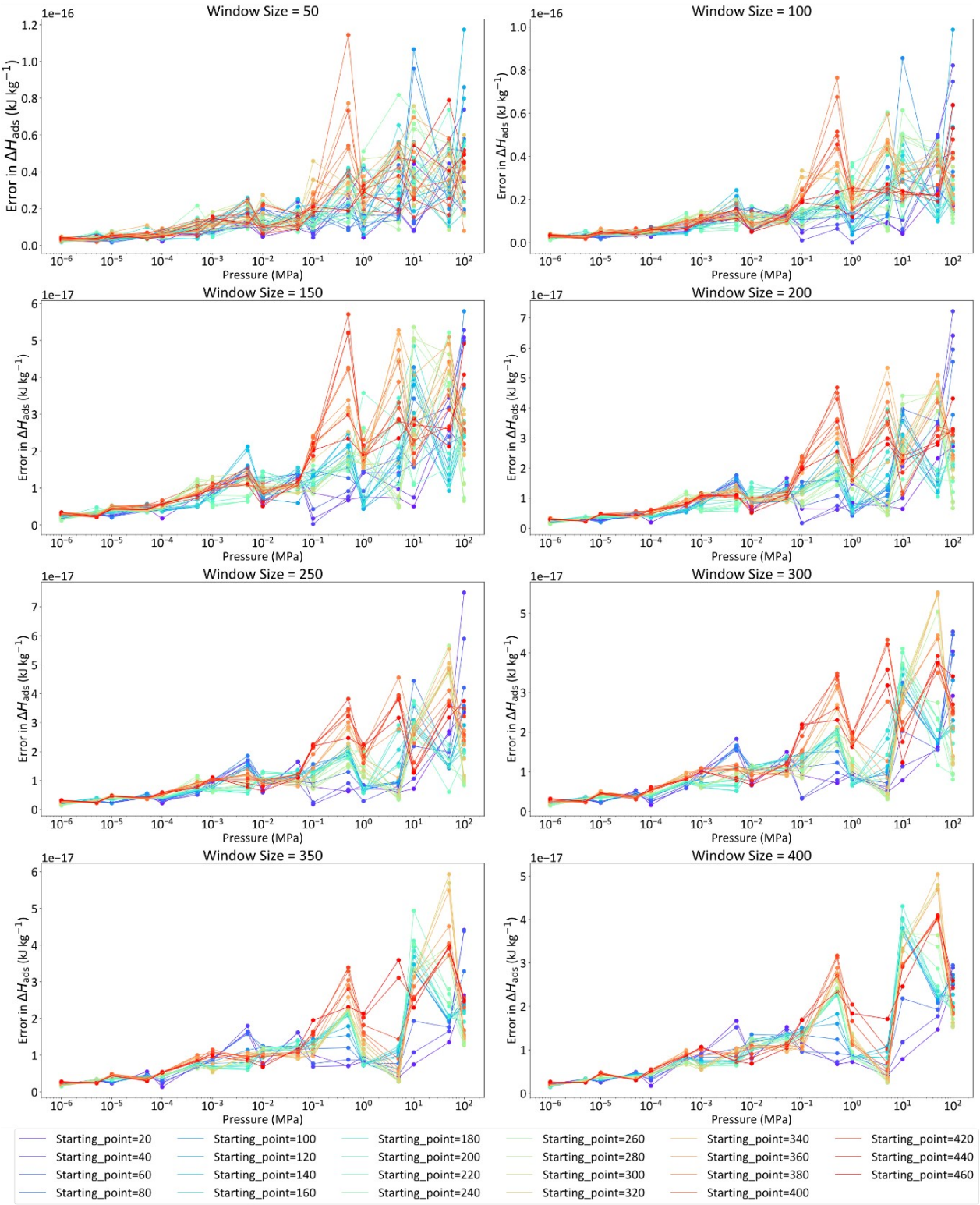


**Figure S22**: Calculated uncertainties in the enthalpies of adsorption of water based on the number of data points considered (window size) and the part of the production run that the data points were taken from.

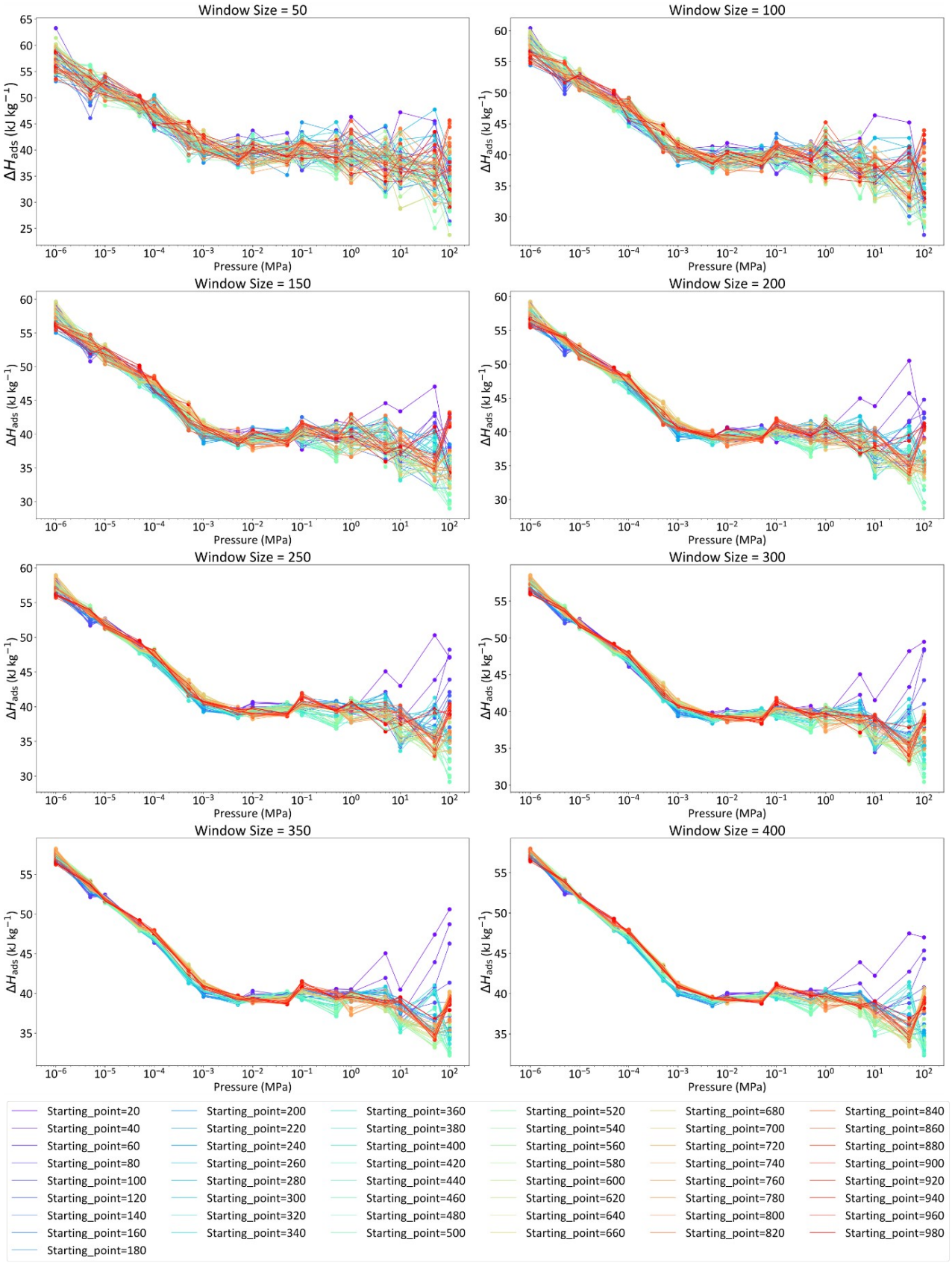


**Figure S23**: Calculated enthalpies of adsorption of carbon dioxide based on the number of data points considered (window size) and the part of the production run that the data points were taken from.

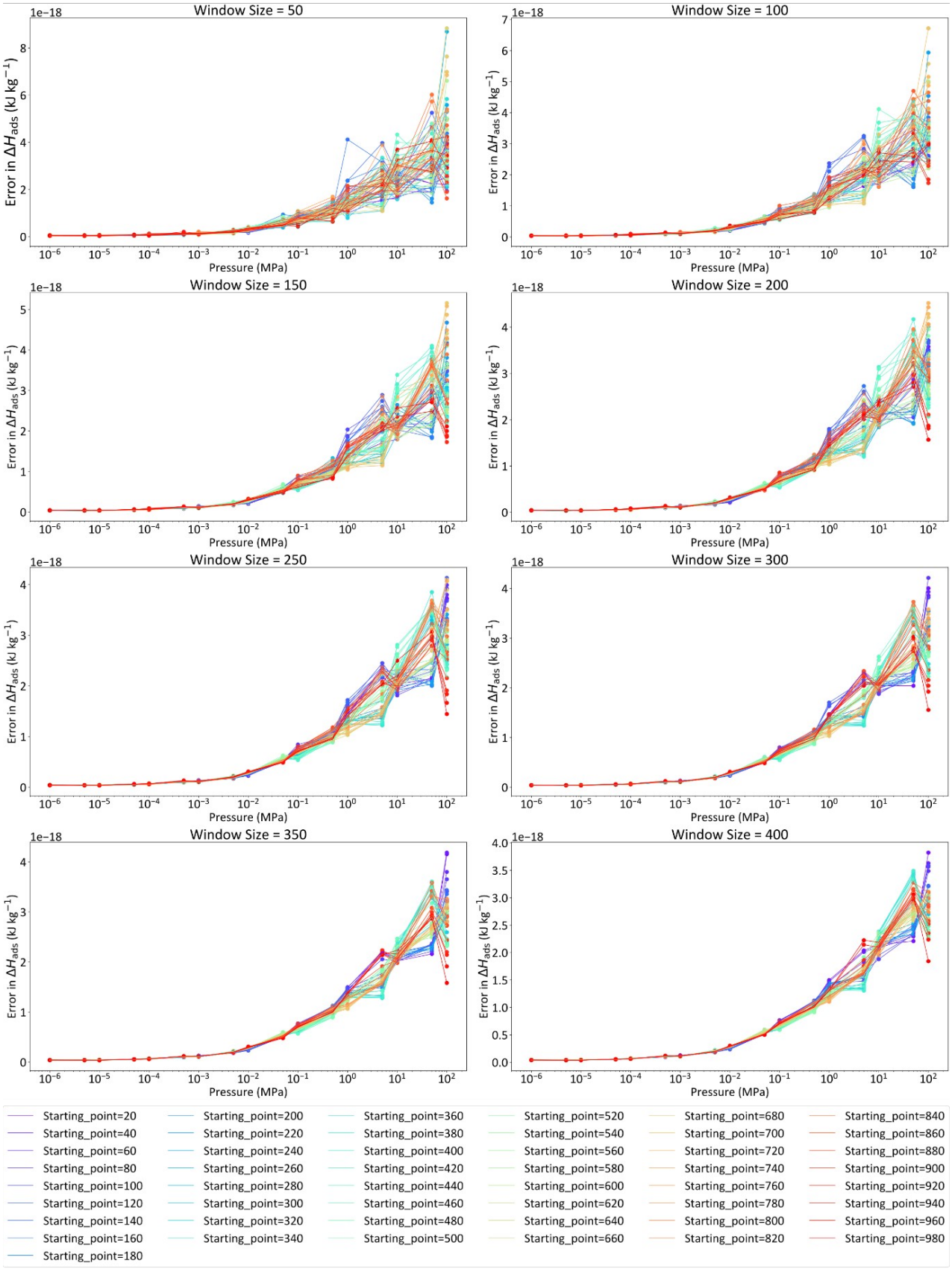


**Figure S24**: Calculated enthalpies of adsorption of carbon dioxide based on the number of data points considered (window size) and the part of the production run that the data points were taken from.

## Section 11: Calculating entropy changes with respect to pressure

Based on the plots shown in S21-24, it is evident that were still large fluctuations from both the potential energy and the number of adsorbed guests that highly vary the resulting value of the heat of adsorption calculated.

From Fig. S21 and Fig. S23, the heat of adsorption was calculated from different sliding sampling window sizes as well as where in the equilibrated trajectories the windows were taken from. As a result, for each simulated pressure, a distribution of enthalpies was obtained, an example can be seen in Fig. S25. d*H* was then taken as the average of these steps and the error was taken as the variation in the values, mathematically taken as the standard deviation (see Fig. S26). With this method, the error obtained represents the lower bound.

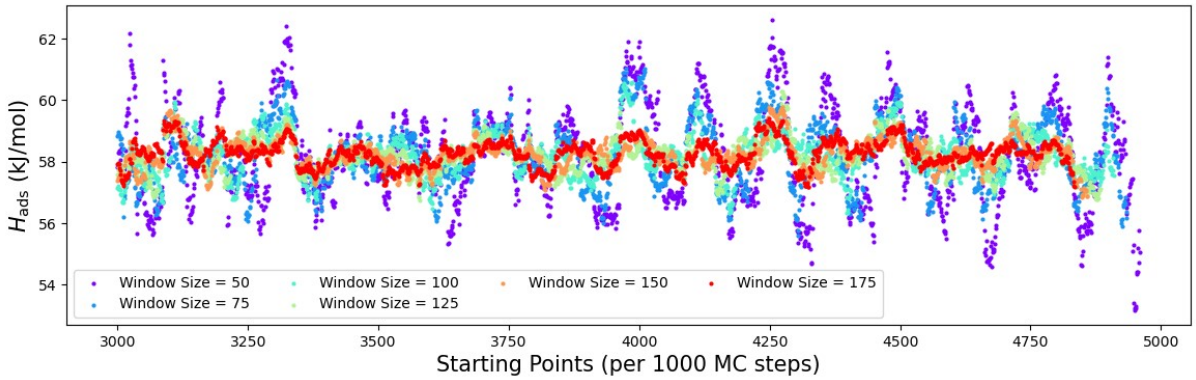


**Figure S25**: At *P* = 1 Pa, the calculated entropy of adsorption of carbon dioxide from different window sizes along the equilibrated GCMC steps.

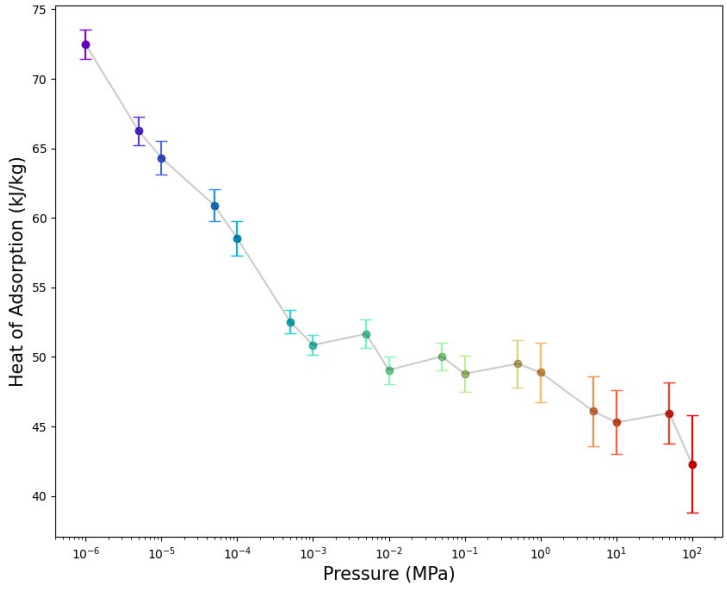


**Figure S26**: d$H_{ads}$ values calculated for the adsorption of $CO_2$ in the MIL-53(Ga)-fum(*c*) framework.

The method of deriving the total entropy change with respects to the change in pressure is shown below. The example data derived from the set of simulations where carbon dioxide was used as the single component guest molecule. From using equations 1-4 from the main text, the entropy changes with respects to the gain or loss of one guest molecule, and the number of guest molecules adsorbed at a given pressure can be visualised as seen in Fig S27.

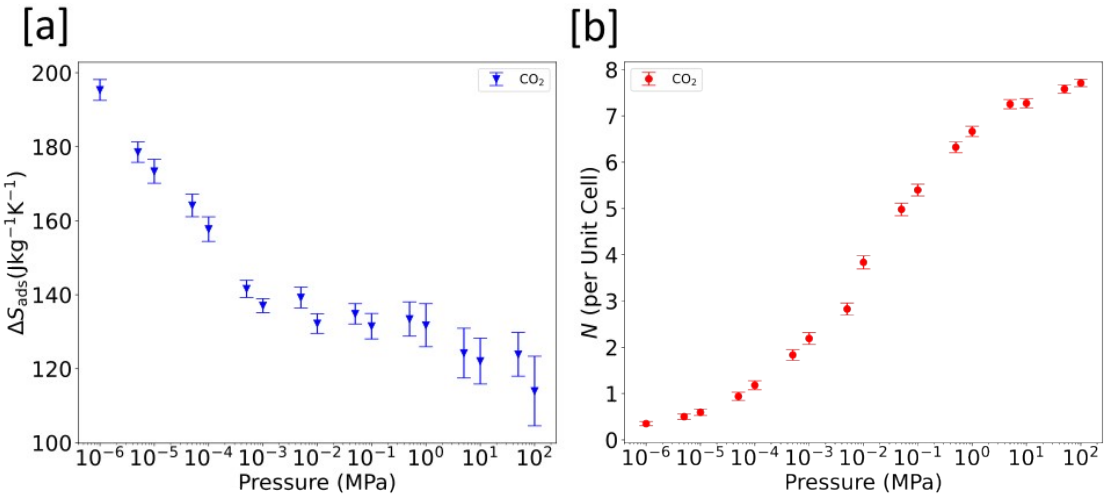


**Figure S27**: [a] Calculated entropy of adsorption of carbon dioxide at a given pressure. [b] Calculated number of molecules of carbon dioxide adsorbed at a given pressure.

As both plots shown in Fig. S27 share a common axis which is pressure, then one may infer the entropy change from a change in number of molecules by plotting the y-axis of the plots against each other. This is illustrated in Fig. S28.

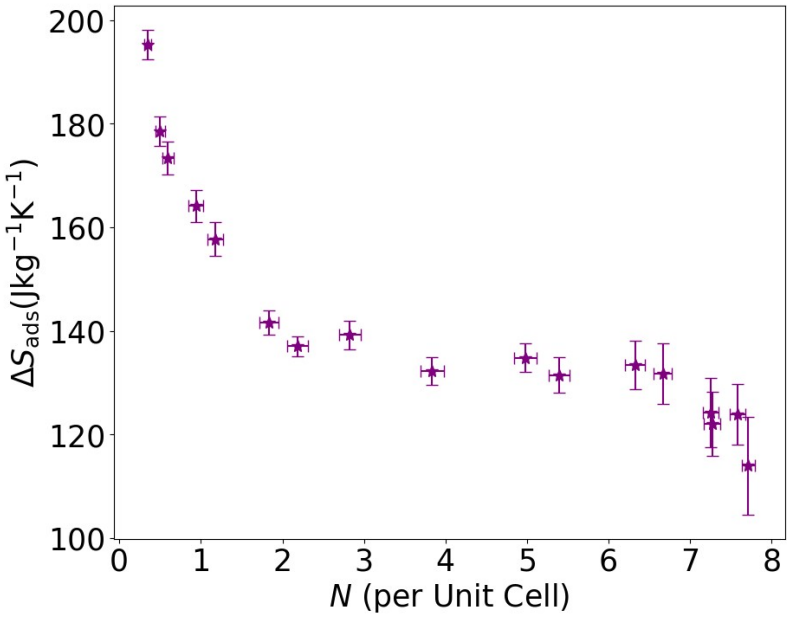


**Figure S28**: Plotting the entropy change against the number of guest molecules present, where each point represents a distinct pressure.

When going from one pressure point to another, as the change in the number of adsorbed molecules is greater than one, the entropy also varies. The resulting total entropy change was calculated using the trapezoidal rule where the subintervals and number of steps must be sufficiently large enough for the integration to converge. Finally, to obtain a range of entropy changes with changes in pressure from ambient, the integrals are then summed, as implemented using the chain trapezoidal rule.

To account for the errors in the entropy change as well as in the number of molecules adsorbed (shown in Fig. S28), the uncertainties in each were propagated as seen in Equations S1 and S2 below. Wherein, Eqn. S1 demonstrate the propagation of error for the change in change in the number of molecules adsorbed between 2 pressure points.

$$\sigma_{dN} = \sqrt{\sigma_{N(P_1)}^{2} + \sigma_{N(P_2)}^{2}} \tag{S1}$$

Following, the error in the total entropy change as a result of the change in pressure (captured by the change in the number of adsorbed molecules) were propagated in consideration of the trapezoid rule:

$$\sigma_{\Delta S_{tot}} = \sqrt{\frac{1}{2}\left(N_{P_2} - N_{P_1}\right)^2\left(\sigma_{\Delta S_{ads,\,P_2}}^{2} + \sigma_{\Delta S_{ads,\,P_1}}^{2}\right) + \frac{1}{2}\left(\Delta S_{ads,\,P_2} + \Delta S_{ads,\,P_1}\right)^2\left(\sigma_{\Delta N_{P_2}}^{2} + \sigma_{\Delta N_{P_1}}^{2}\right)} \tag{S2}$$

While the above, holds for adjacent pressure steps, for pressure steps in combination, the error was then propagative with the additive/subtractive propagation equation.

The calculated entropy change as a result in a change in gaseous pressure for the desorption of water or carbon dioxide is shown in Table S4. This corresponds to "depressurisation" from ambient conditions of 1 bar. The entropy change corresponding to the adsorption of water or carbon dioxide by an increase in gaseous pressure is shown in Table S5.

**Table S4**: The calculated entropy changes with respects to the changes in pressure for the adsorption of water and carbon dioxide in the MIL-53(Ga)-fum(*c*) framework. The change in pressure were taken with 0.1 MPa as the reference point. The changes in pressure seen in the table for the gaseous depressurisation of the framework from ambient pressure (0.01 MPa).

| **Depressurising from ambient** | | |
|---|---|---|
| $\Delta P$ **(MPa)** | $\Delta S_{tot}$ **(J K$^{-1}$ kg$^{-1}$)** | |
| | Water | Carbon Dioxide |
| -0.04 | -410(30) | -340(30) |
| -0.045 | -480(40) | -510(40) |
| -0.049 | -710(50) | -620(50) |
| -0.0495 | -820(60) | -680(60) |
| -0.0499 | -1080(70) | -810(70) |
| -0.04995 | -1170(80) | -850(70) |
| -0.04999 | -1510(90) | -930(80) |
| -0.049995 | -1600(100) | -950(80) |
| -0.049999 | 1900(100) | -980(80) |

**Table S5**: The calculated entropy changes with respects to the changes in pressure for the adsorption of water and carbon dioxide in the MIL-53(Ga)-fum(*c*) framework. The change in pressure were taken with 0.1 MPa as the reference point. The changes in pressure seen in the table for the gaseous pressurisation of the framework from ambient pressure (0.01 MPa).

| **Pressurising from ambient** | | |
|---|---|---|
| $\Delta P$ **(MPa)** | $\Delta S_{tot}$ **(J K$^{-1}$ kg$^{-1}$)** | |
| | Water | Carbon Dioxide |
| 0.4 | 210(30) | 150(30) |
| 0.9 | 210(40) | 210(40) |
| 4.9 | 320(40) | 300(50) |
| 9.9 | 330(50) | 310(50) |
| 49.9 | 340(50) | 350(50) |
| 99.9 | 370(50) | 370(60) |

The data shown in Table S4 and S5 are plotted and shown in Fig. S29 and 30, to represent the increase or decrease in pressure applied to the system from ambient conditions.

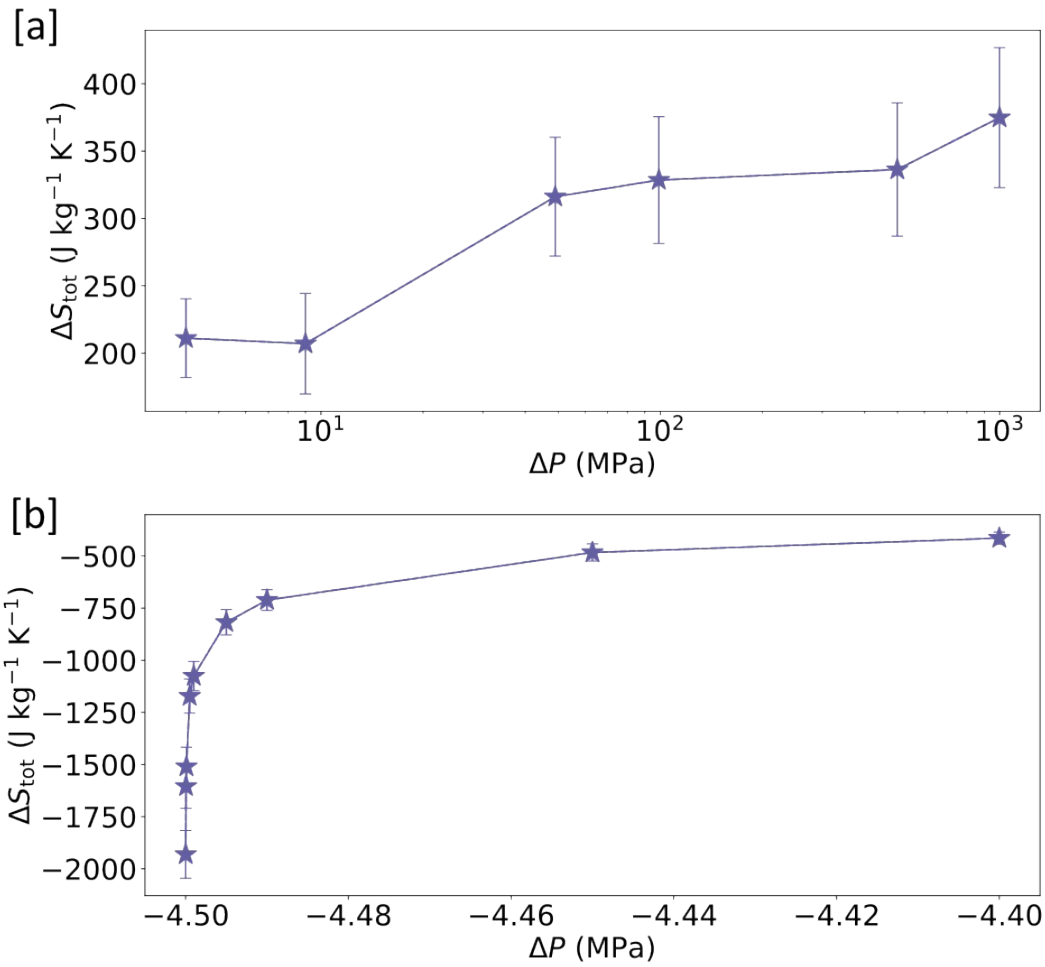


**Figure S29**: The calculated entropy changes corresponding the adsorption of water molecules in MIL-53(In)-fum(*c*) wherein the change in the number of molecules adsorbed is dictated by the change in the simulated pressures. The entropy changes are plotted against the [a] increase or [b] decrease in pressures from atmospheric pressure (0.1 MPa).

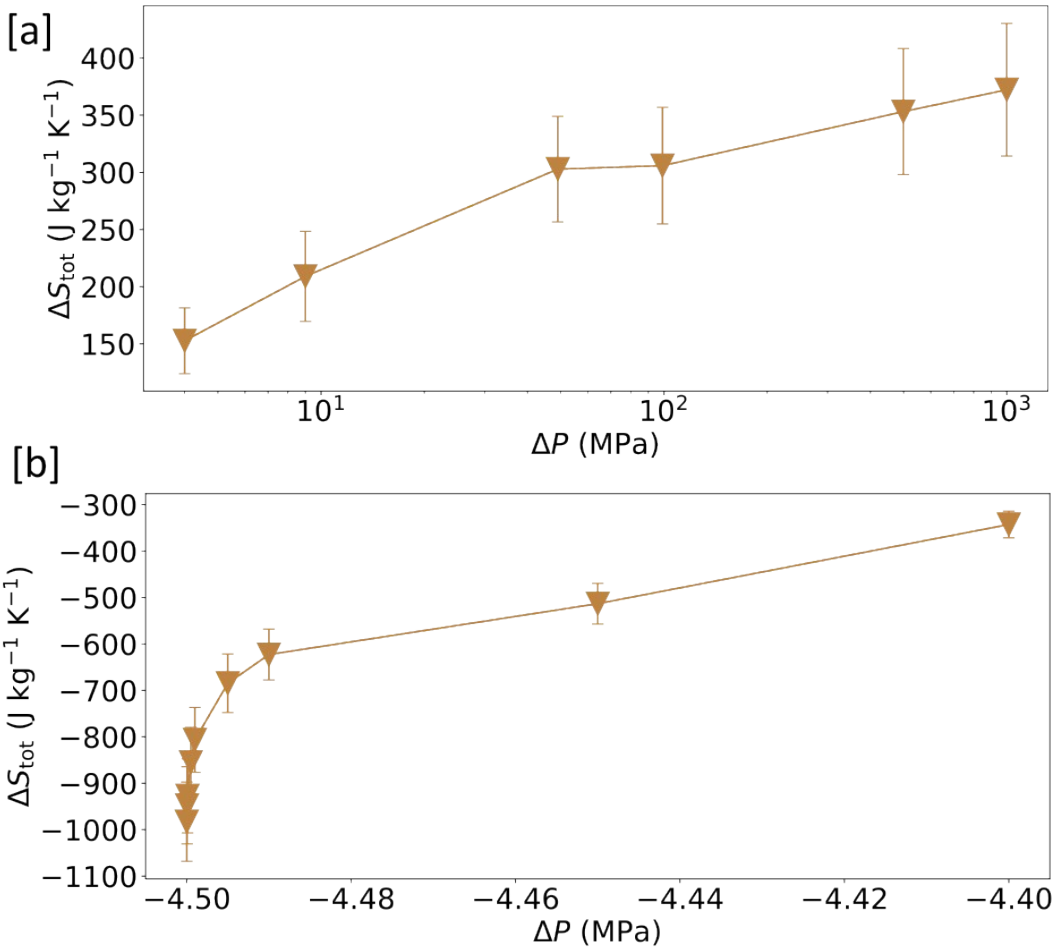


**Figure S30**: The calculated entropy changes corresponding the adsorption of carbon dioxide molecules in MIL-53(In)-fum(*c*) wherein the change in the number of molecules adsorbed is dictated by the change in the simulated pressures. The entropy changes are plotted against the [a] increase or [b] decrease in pressures from atmospheric pressure (0.1 MPa).

## Section 12: SCRXD raw data, simulation inputs, and analysis programs

The raw data from the SCRXD, everything used to obtain the results shown in this publication, and the analysis programs that was written as part of this research are available, open source, on the GitHub (https://github.com/hobdaylab/Codes_MIL-53-Ga-fum_paper).

Section 13: Experimental Characterisation of MIL-53(Ga)-fum*(b)* and MIL-53(In)-fum*(c)*

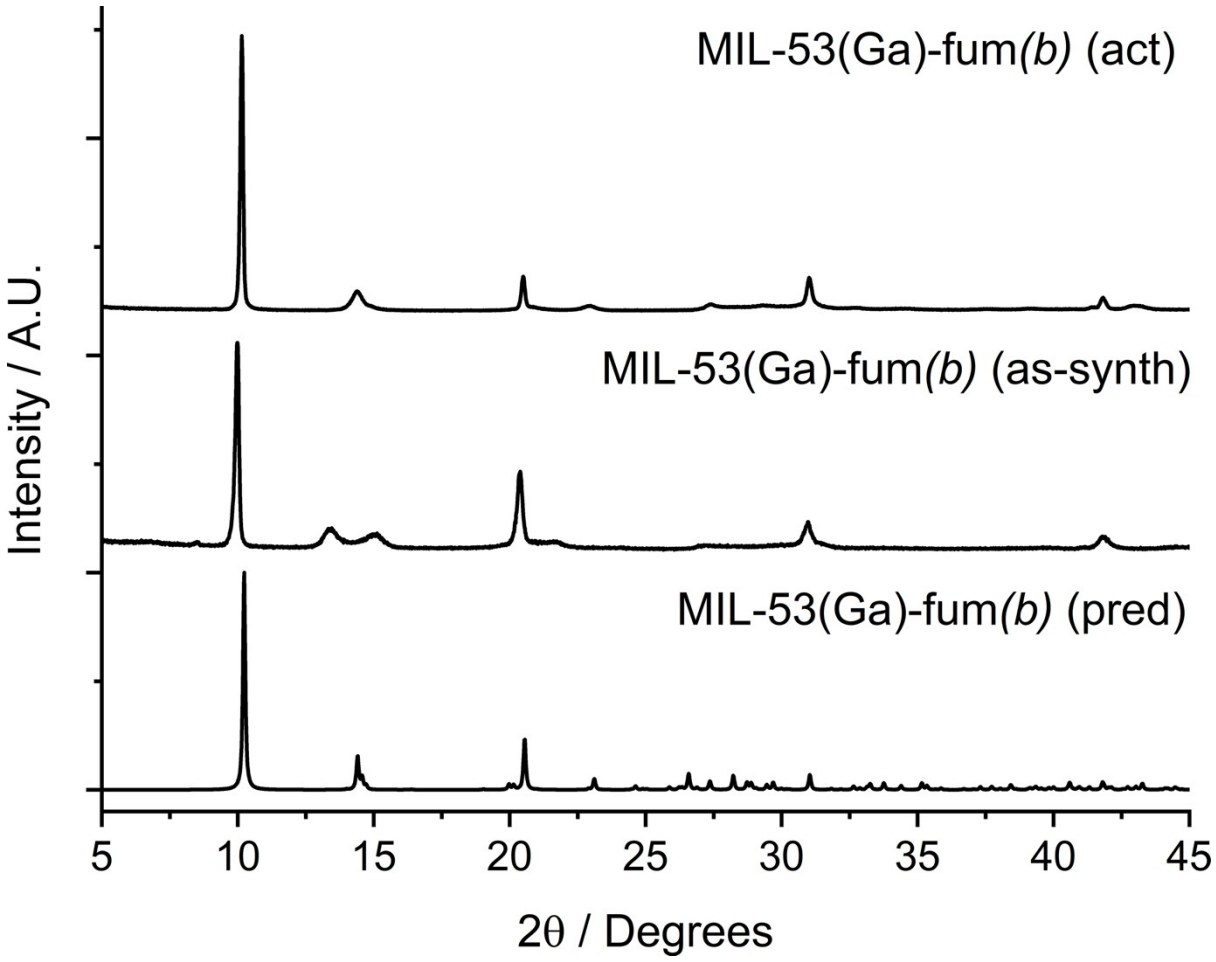


**Figure S31.** Stacked partial powder X-ray diffractograms of MIL-53(Ga)-fum*(b)* in the as-synthesised and activated forms, compared with that predicted from the Rietveld refined structure reported by Zhang *et al.*, highlighting the rigidity of the MOF.[1]

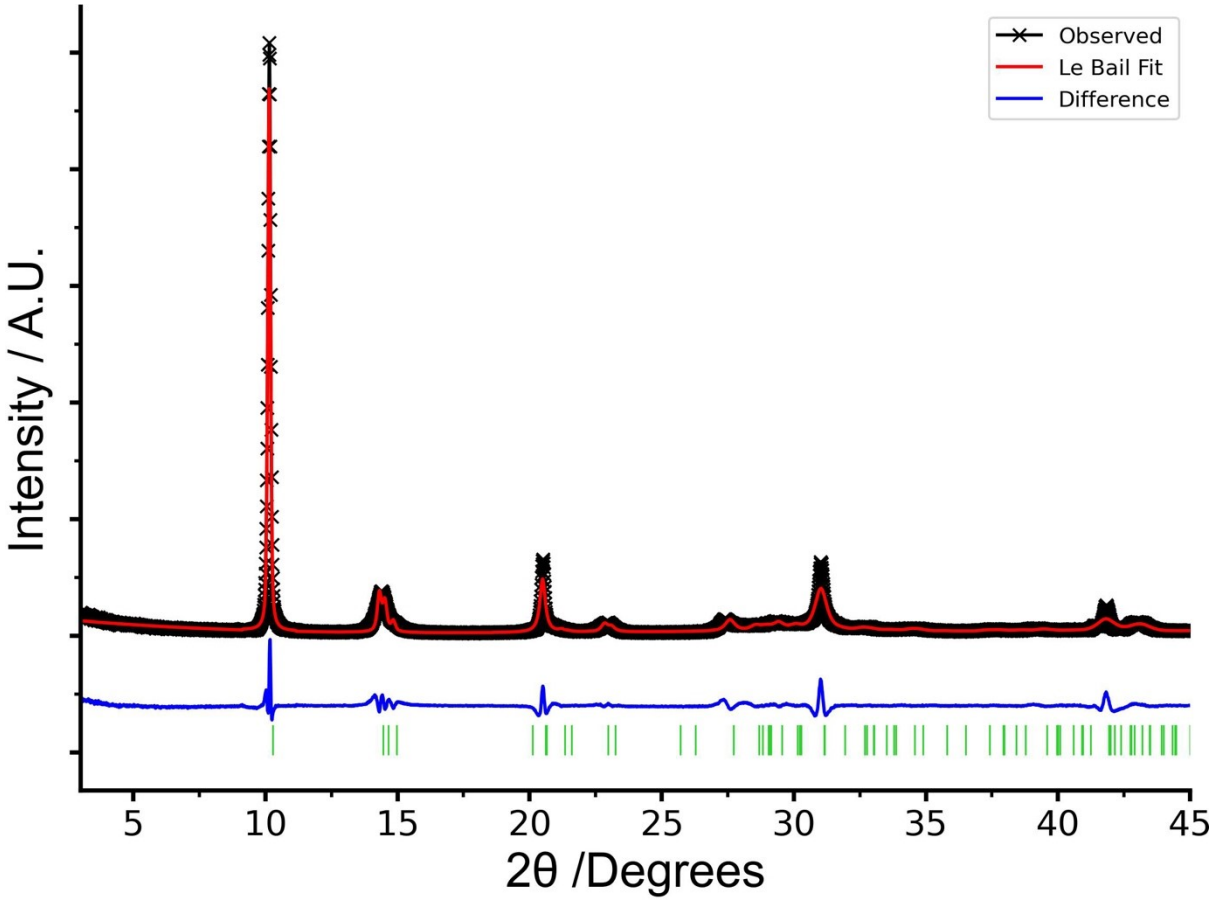


**Figure S32.** Le Bail fit of the powder X-ray diffractogram of activated MIL-53(Ga)-fum*(b)*. *I*2/*a*; *a* = 6.80061 Å, *b* = 12.07899 Å, *c* = 12.29090 Å, β = 94.58628 °, *V* = 1006.434 Å; $R_p$ = 12.65, w$R_p$ = 17.60.

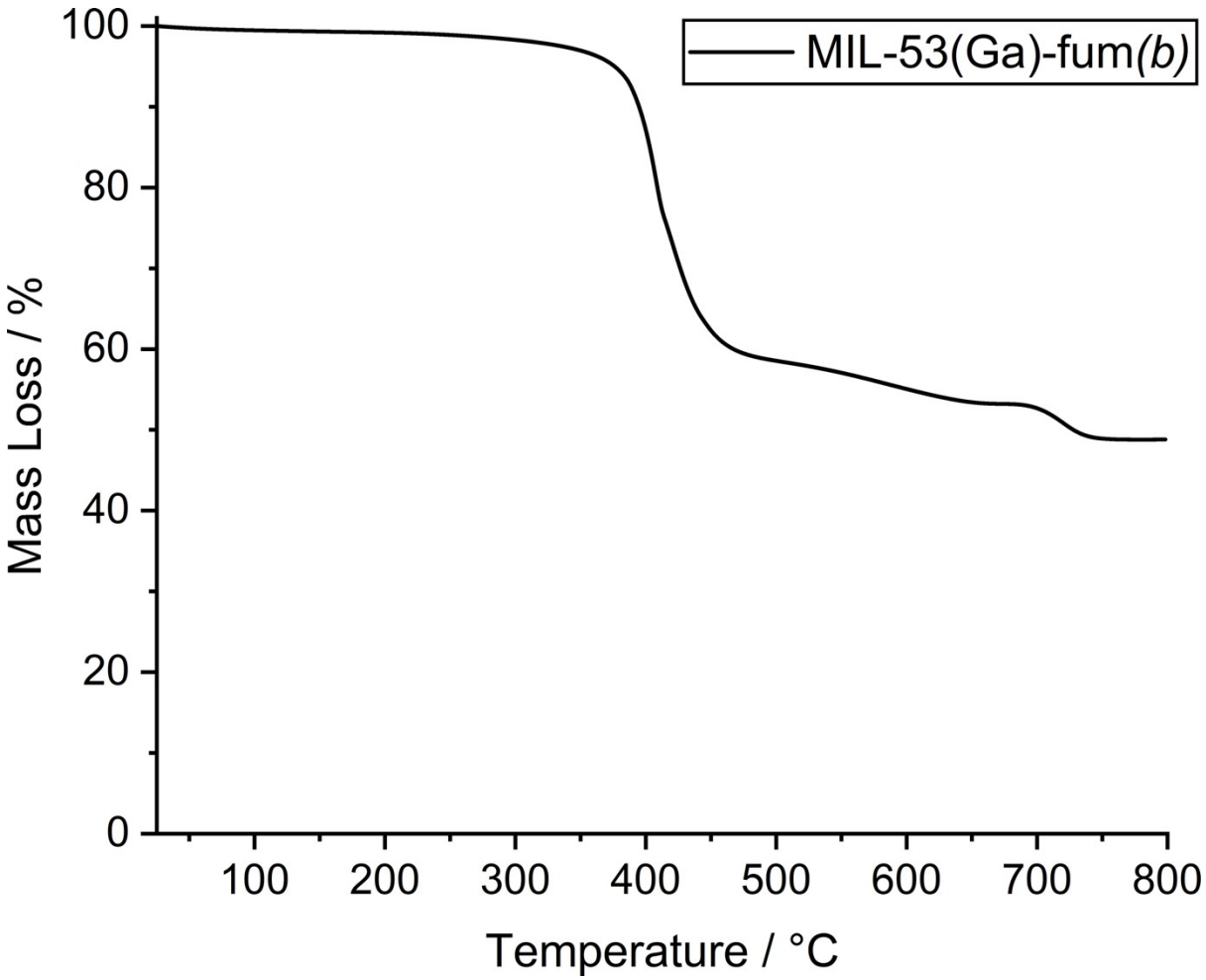


**Figure S33.** Thermogravimetric analysis (in air) of activated MIL-53(Ga)-fum*(b)*.

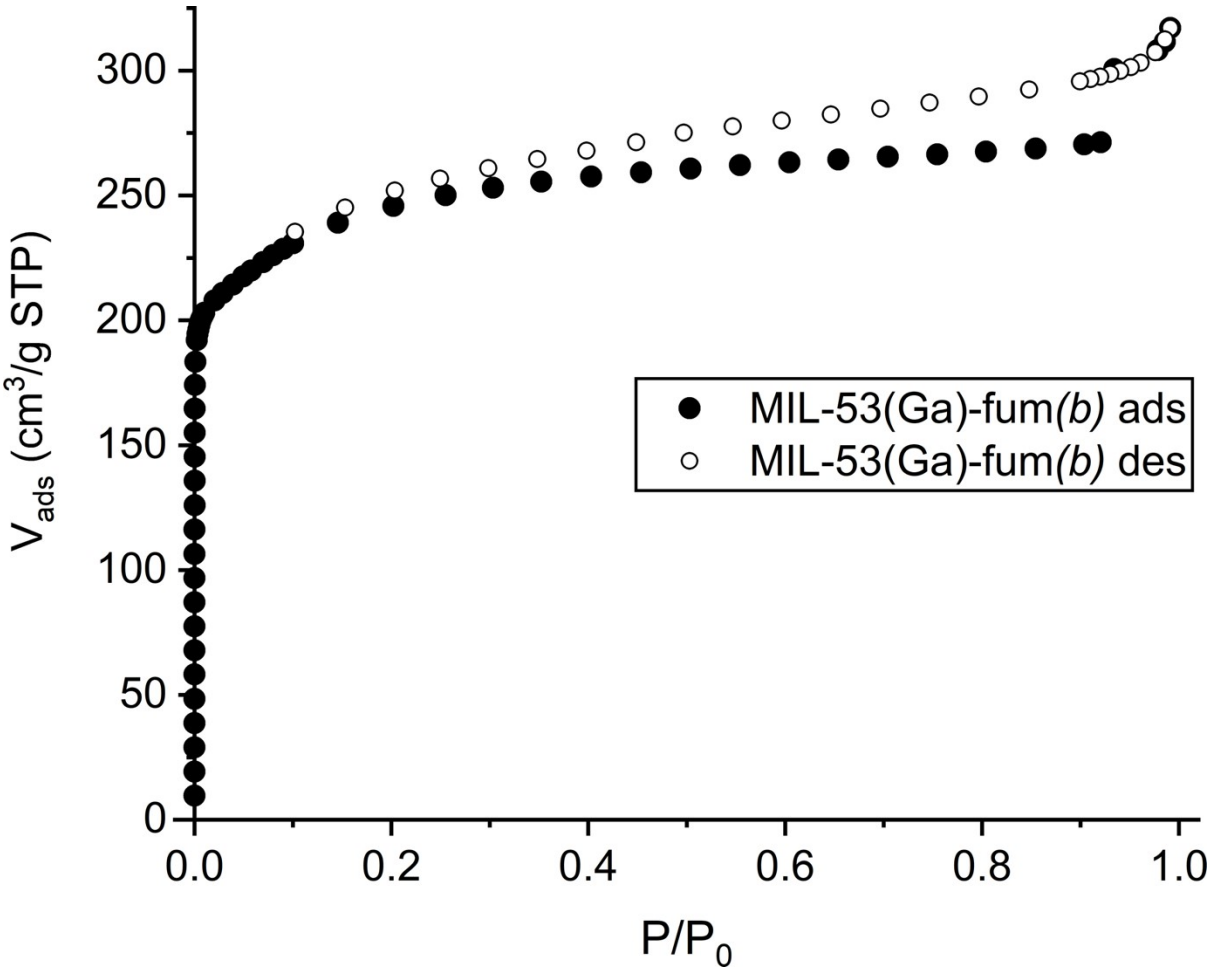


**Figure S34.** $N_2$ adsorption/desorption isotherm (77 K) for activated MIL-53(Ga)-fum*(b)*.

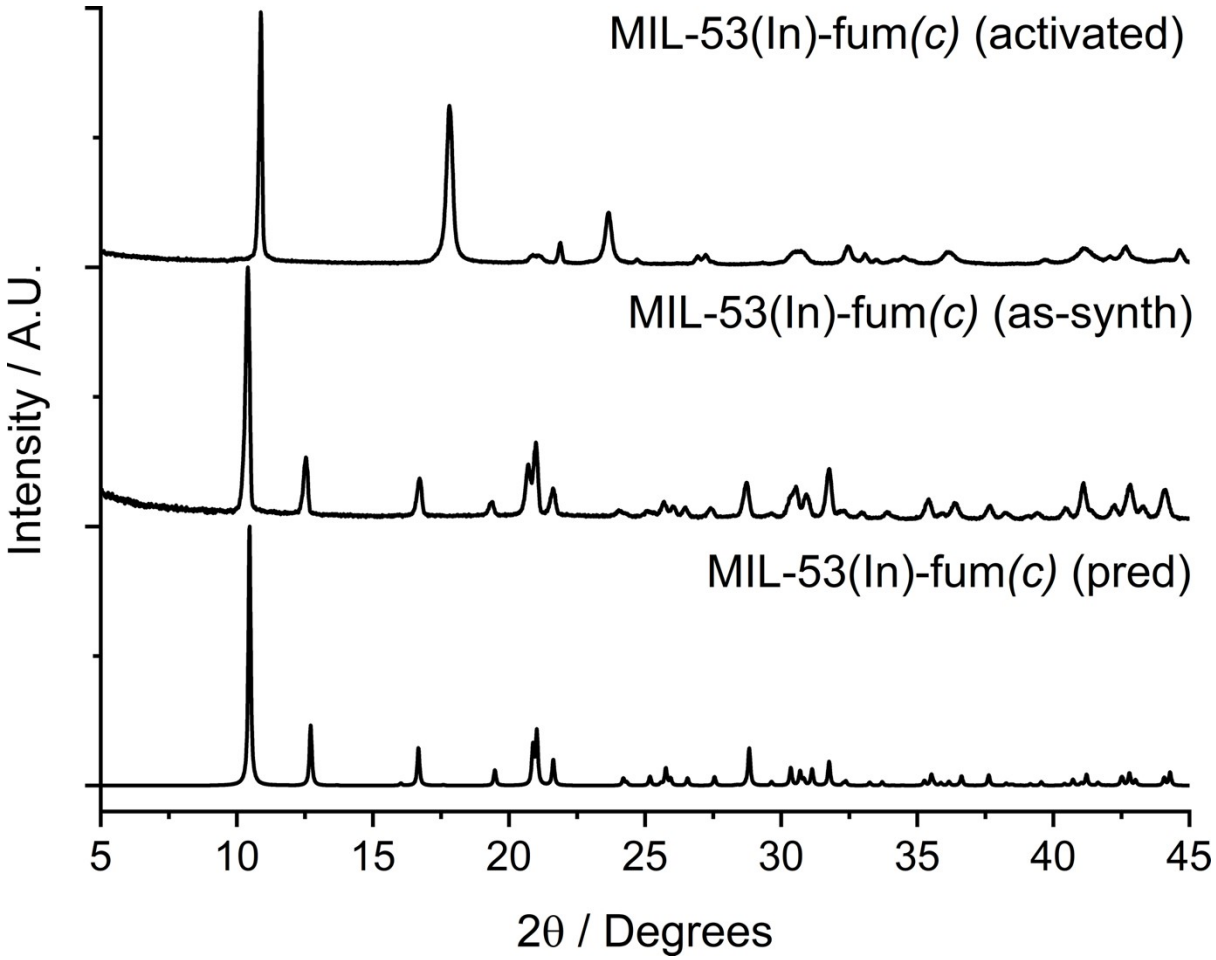


**Figure S35.** Stacked partial powder X-ray diffractograms of MIL-53(In)-fum*(c)* in the as-synthesised and activated forms, compared with that predicted from our crystal structure reported herein. The activated sample has a considerably different diffractogram consistent with closing.

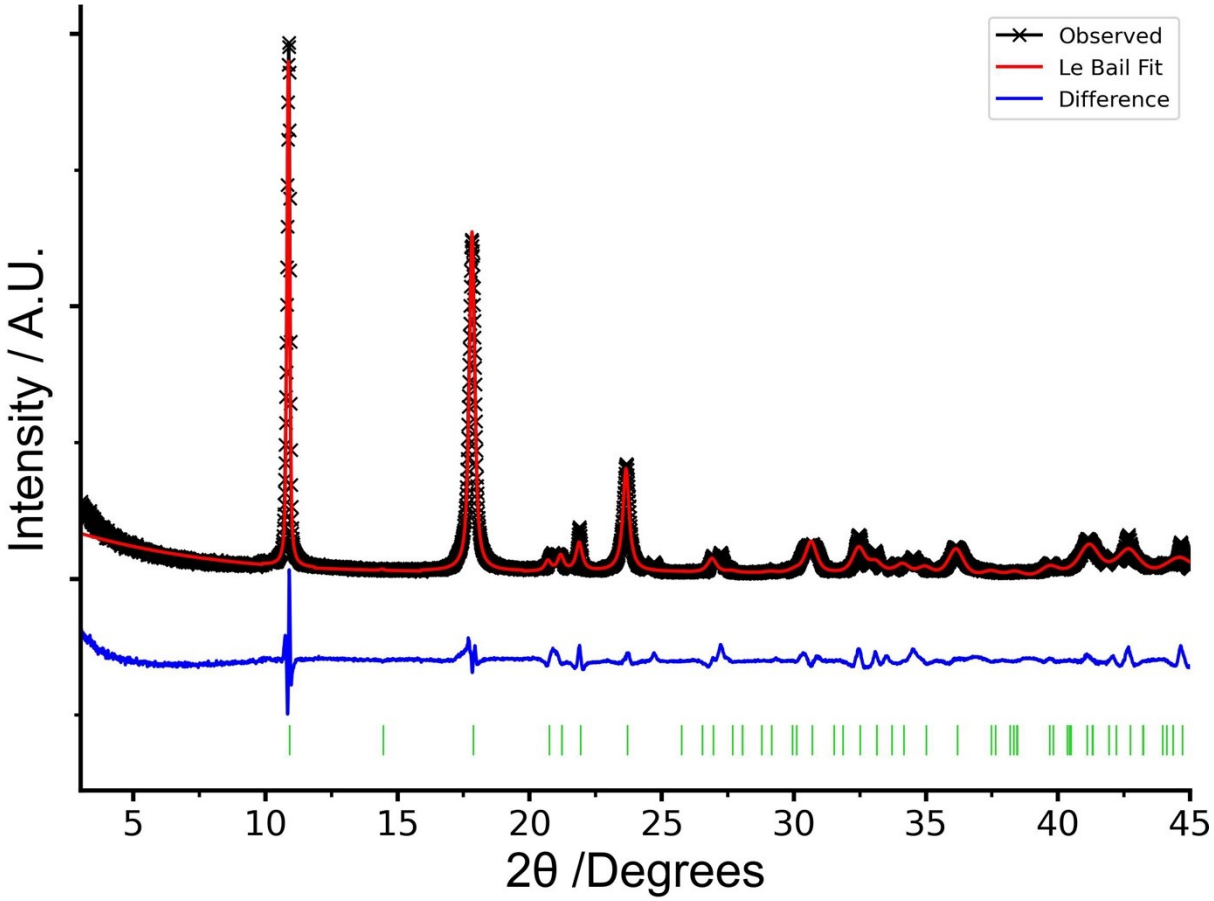


**Figure S36.** Le Bail fit of the powder X-ray diffractogram of activated MIL-53(In)-fum*(c)*. *I*2/*a*; *a* = 7.5101 Å, *b* = 6.6124 Å, *c* = 16.2290 Å, β = 92.2146 °, *V* = 804.726 Å; $R_p$ = 13.5, w$R_p$ = 17.5. The decreased unit cell volume is highly consistent with the structure closing.

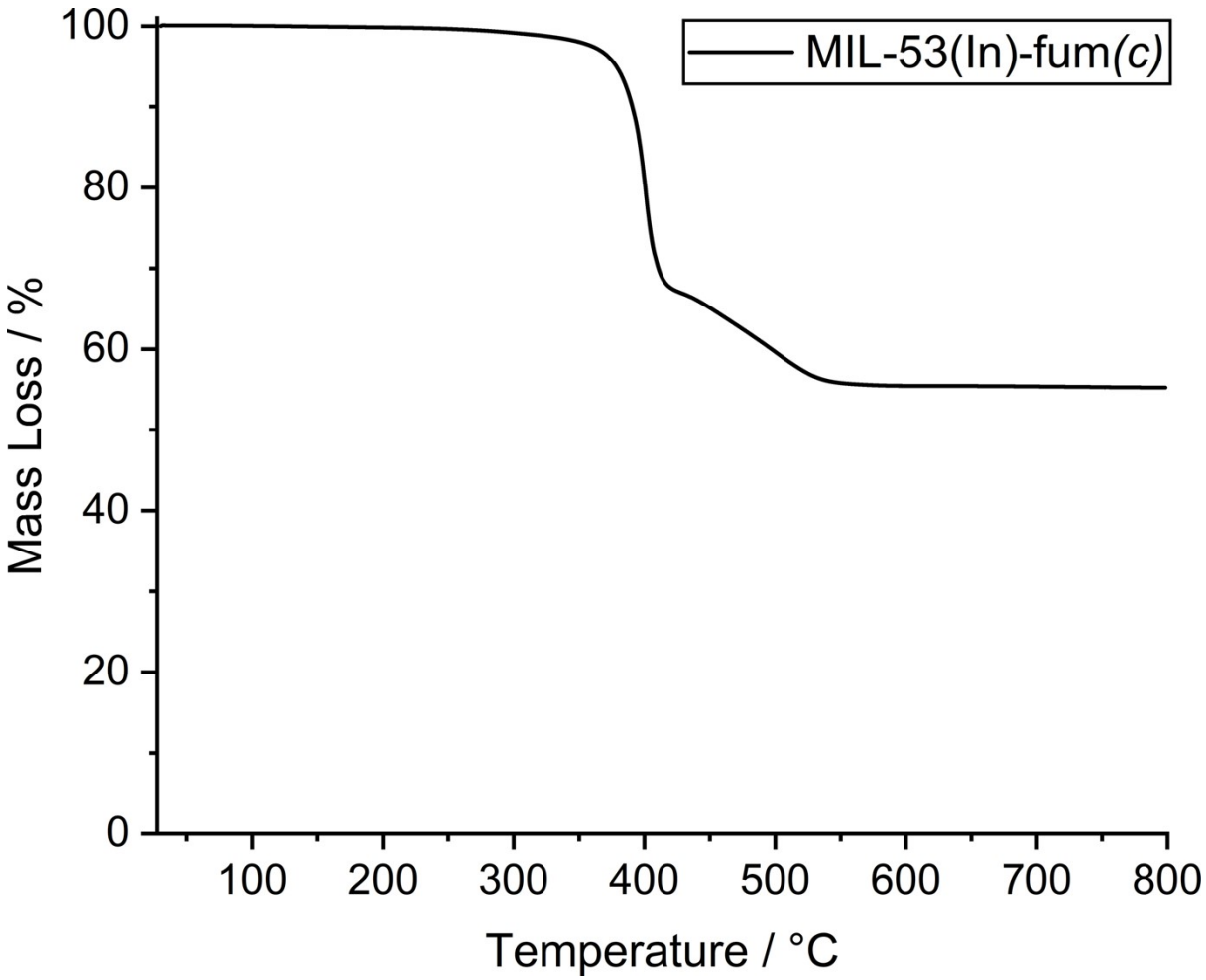


**Figure S37.** Thermogravimetric analysis (in air) of activated MIL-53(In)-fum*(c)*.

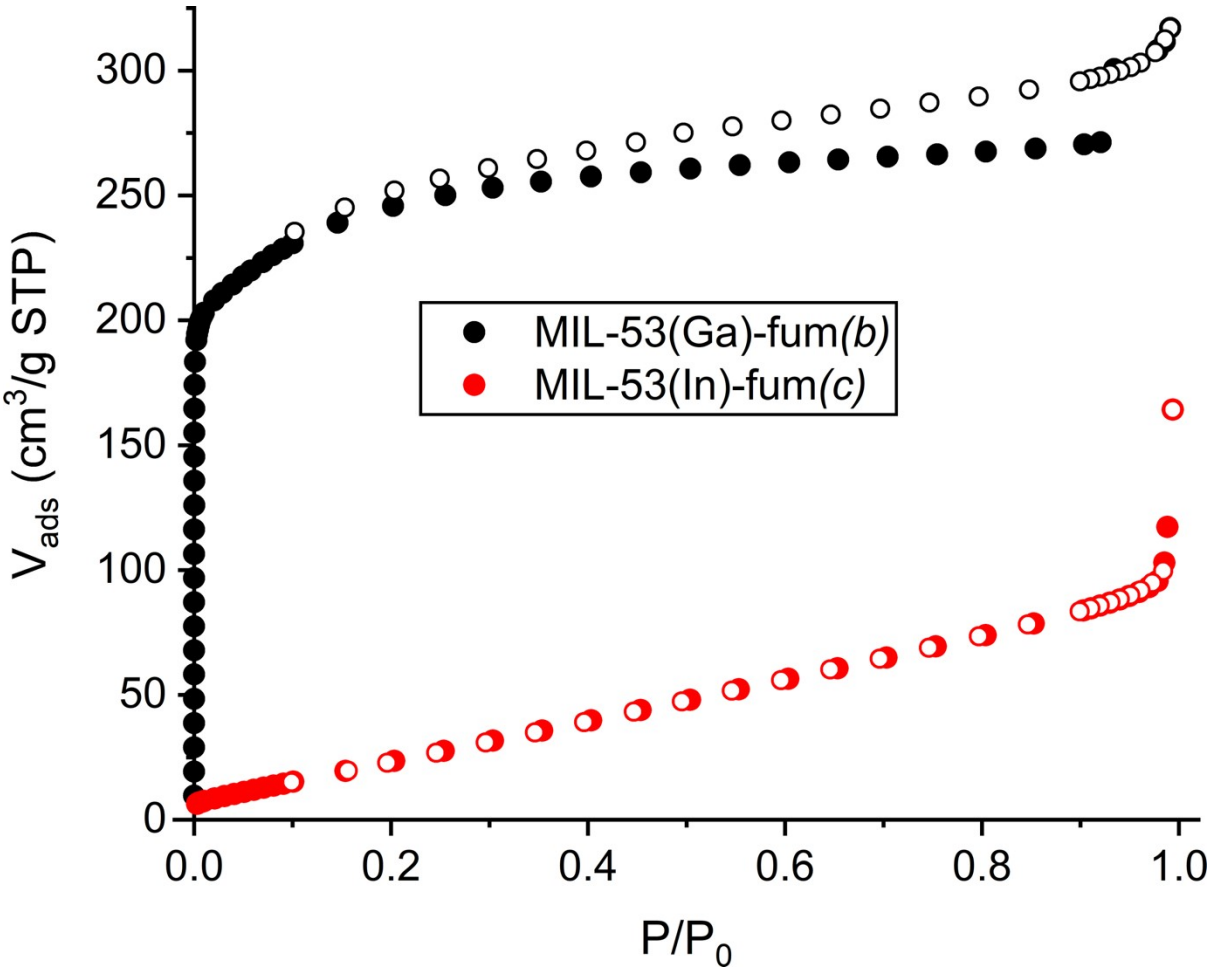


**Figure S38.** $N_2$ adsorption/desorption isotherms (77 K) for activated MIL-53(In)-fum*(c)* (black) compared to activated MIL-53(Ga)-fum*(b)* (black). The lack of porosity (and lack of residual solvent in the TGA) is consistent with the closing of MIL-53(In)-fum*(c)* upon activation.

## Section 14: Pore Analysis Settings

The inputs, alongside the structure of the MOF and unit cell parameters, given to PoreBlazer v4.0.0 are as follows:

```
UFF.atoms
2.58, 10.22, 298, 12.8
3.314
500
0.2
20.0, 0.25
21908391
0
! Default forcefield: UFF
! Helium atom sigma (A), helium atom epsilon (K), temperature (K), cutoff distance (A)
! Nitrogen atom sigma (A)
! Number of samples per atom for the surface area calculation
! 0.2: Cubelet size (A)
! Largest anticipated pore diameter (A), size of the bin for PSD (A)
! Random number seed
! Visualization options: 1 -xyz, 2 - grd, 3 - both; 0 - none
```

The UFF parameters for the atoms were given as:

```
Ga    3.905  208.69 69.723
C     3.431   52.8    12.0
O     3.118   30.2    16.0
H     2.571   22.14   1.0
```

## Section 15: Reference

1 Y. Zhang, B. E. G. Lucier, S. M. McKenzie, M. Arhangelskis, A. J. Morris, T. Friščić, J. W. Reid, V. V. Terskikh, M. Chen and Y. Huang, *ACS Appl. Mater. Interfaces*, 2018, **10**, 28582–28596.